Finding the magnetopause location using soft X-ray observations and a statistical inverse method

Gonzalo Cucho-Padin[1,2]*, Hyunju Connor[3], Jaewoong Jung[3,4], Brian Walsh[5], and David G. Sibeck[1]

[1]Space Weather Laboratory, NASA Goddard Space Flight Center, Greenbelt, MD, USA;

[2]Department of Physics, The Catholic University of America, Washington, DC, USA;

[3]Geospace Physics Laboratory, NASA Goddard Space Flight Center, Greenbelt, MD, USA;

[4]Astronomy Department, University of Maryland College Park, College Park, MD, USA;

[5]Center for Space Physics, Department of Mechanical Engineering, Boston University, Boston, MA, USA

Key Points:

- A method for finding the magnetopause location based on statistical inverse theory and soft X-ray magnetosheath emissions is presented.
- Instrument orbit and attitude from the upcoming NASA LEXI mission are used to demonstrate technique feasibility.
- Results show that the inverse method is robust against Poisson-distributed shot noise in images, but its accuracy relies heavily on vantage points and the prior model.

Citation: Cucho-Padin, G., Connor, H., Jung, J., Walsh, B., and Sibeck, D. G. (2024). Finding the magnetopause location using soft X-ray observations and a statistical inverse method. *Earth Planet. Phys.*, *8*(1), 184–203. http://doi.org/10.26464/epp2023070

Abstract: Variability in the location and shape of the dayside magnetopause is attributed to magnetic reconnection, a fundamental process that enables the transfer of mass, energy, and momentum from the solar wind into the magnetosphere. The spatial and temporal properties of the magnetopause, under varying solar and magnetospheric conditions, remain largely unknown because empirical studies using in-situ observations are challenging to interpret. Global wide field-of-view (FOV) imaging is the only means to simultaneously observe the spatial distribution of the plasma properties over the vast dayside magnetospheric region and, subsequently, quantify the energy transport from the interplanetary medium into the terrestrial magnetosphere. Two upcoming missions, ESA/CAS SMILE and NASA's LEXI will provide wide-field imagery of the dayside magnetosheath in soft X-rays, an emission generated by charge exchange interactions between high charge-state heavy ions of solar wind origin and exospheric neutral atoms. High-cadence two-dimensional observations of the magnetosheath will allow the estimation of dynamic properties of its inner boundary, the magnetopause, and enable studies of its response to changes in the solar wind dynamic pressure and interplanetary magnetic field orientation. This work introduces a statistically-based estimation approach based on inverse theory to estimate the spatial distribution of magnetosheath soft X-ray emissivities and, with this, identify the location of the magnetopause over the Sun–Earth line. To do so, we simulate the magnetosheath structure using the MHD-based OpenGGCM model and generate synthetic soft X-ray images using LEXI's orbit and attitude information. Our results show that 3-D estimations using the described statistically-based technique are robust against Poisson-distributed shot noise inherent to soft X-ray images. Also, our proposed methodology shows that the accuracy of both three-dimensional (3-D) estimation and the magnetopause standoff distance calculation highly depends on the observational point.

Keywords: magnetopause; soft X-ray; tomography

1. Introduction

The Earth's magnetopause is defined as the boundary between the terrestrial and interplanetary magnetic fields (IMFs). Observations of the motion of the dayside magnetopause in response to changes in the IMF orientations have been associated with magnetic reconnection, a crucial mechanism that transports mass, momentum, and energy from the solar wind into the terrestrial

magnetosphere (Aubry et al., 1970; Sibeck et al., 2018). Due to its significance for the heliophysics science community, several in-situ investigations of magnetic reconnection occurrence have been performed in the last decade (e.g., using NASA's THEMIS and MMS data). However, these measurements are still difficult to interpret because only a limited number of missions cover the vast extent of the magnetopause and because subtle variations in solar wind parameters can abruptly change reconnection locations. In recent years, optical remote sensing of soft X-ray emissions has aroused the interest of the magnetospheric community as a means for global imaging of the dayside magnetosheath (Robert-

son and Cravens, 2003; Kuntz et al., 2015; Connor et al., 2021). Within the near-Earth region, soft X-ray photons are generated through charge exchange interactions between solar wind ions, specifically high charge state heavy ions, and exospheric neutral hydrogen (H) atoms. Equation (1) shows an example of this interaction where the solar wind ion O^{7+} picks up the electron of the H atom and produces O^{6+}, a proton, and a soft X-ray photon with energy $\approx$560 eV.

$$O^{7+} + H \rightarrow O^{6+} + H^+ + h\nu . \tag{1}$$
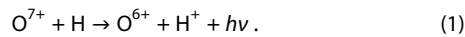
The soft X-ray emissions range from 100 to ~2000 eV, where the electron-volt (eV) unit is associated with the photon wavelength (Sibeck et al., 2018).

In the following years, two missions will image the dayside magnetosphere in soft X-rays: the European Space Agency/ Chinese Academy of Science (ESA/CAS) Solar wind Magnetosphere Ionosphere Link Explorer (SMILE) and NASA's Lunar Environment heliospheric X-ray Imager (LEXI) missions. SMILE will acquire soft X-ray images with its 15.5° × 26.5° wide field-of-view (FOV) imaging sensor from a highly elliptical and highly inclined (polar) orbit with an apogee of 19 Earth radii (R_E) and 52-hour orbital period. On the other hand, LEXI will use its 9.1° × 9.1° FOV to image the dayside magnetosheath for several days from a Lunar-based platform with a nearly circular orbit and close to the ecliptic plane with a ~60 R_E geocentric distance.

To support these upcoming missions and enhance their scientific return, several investigations have been conducted to extract the magnetopause location from simulated soft X-ray observations. For example, Collier and Connor (2018) used synthetic line-of-sights (LOSs) soft X-ray measurements to derive tangent points over the magnetopause (i.e., points where the measured intensity is high and represents the boundary of the magnetosheath) and with these, reconstruct the 3-D cross-section of the magnetopause. Jorgensen et al. (2019a, 2019b) developed a method based on fitting 2-D soft X-ray images to an experimental functional form whose resulting parameters provide information regarding bow shock and magnetopause location. Sun TR et al. (2020) introduced the tangent fitting approach that finds the optimum match between tangent directions derived from a single soft X-ray image and a parameterized magnetopause function. As a result, the magnetopause structure can be reconstructed. Also, Samsonov et al. (2022b) evaluated the use of the tangential direction approach introduced by Collier and Connor (2018) under a realistic scenario that includes SMILE orbit and attitude, as well as the expected photon noise in the 2-D images.

Tomographic estimation is another promising technique to obtain the magnetopause location via estimation of the three-dimensional (3-D) structure of the magnetosheath soft X-ray emissivities and the subsequent detection of its boundaries. The tomographic approach solves a physic-based inverse problem that requires 2-D soft X-ray images of the magnetosheath along with viewing geometry data to retrieve the 3-D soft X-ray emissivity (see more details in Section 2). The accuracy of tomographic retrievals heavily depends on the capability of the imaging sensor to observe the target from different vantage points. For example, computed tomography (CT), developed for medical applications,

can retrieve high-resolution and low-uncertainty estimation results due to the continuous acquisition of data along a circular trajectory around a (semi-) static target (Beister et al., 2012). This is typically termed a full-angle observation geometry. Notwithstanding, for space physics applications and specifically for SMILE and LEXI missions, the use of a single spacecraft moving around large-period orbits, as well as the expected short-term variability of the target's physical properties (e.g., less than 1 hour for the magnetosheath plasma structure), generates a challenging limited-angle observation problem.

To date, two investigations have focused on studying and developing tomographic approaches that deal with limited-angle observations to support the SMILE mission. Jorgensen et al. (2022) conducted a theoretical study of tomographic reconstruction of the magnetosheath using SMILE's orbit and attitude. They simulated SMILE soft X-ray images acquired from the northern hemisphere for a period of 30 hours and utilized the iterative method known as the Algebraic Reconstruction Technique (ART) to perform 3-D reconstructions. To reduce the noise generated by data sparsity, they included several stages of smoothness via Total Variation (TV) regularization. Also, to deal with the limited-angle observation, they assumed a North–South symmetry of the magnetosheath such that observations could be duplicated and located in the opposite hemisphere to ultimately improve the reconstructions. More recently, Wang RC et al. (2023) developed a methodology that uses generative adversarial networks (GANs) to assist tomographic reconstructions by supplementing additional 2-D soft X-ray images from locations not observed by the imaging sensor.

In this manuscript, we propose a statistically-based estimation technique, with foundations on tomography, that will serve to calculate the 3-D structure of the magnetosheath soft X-ray emissivities and, with this, identify the magnetopause location. This technique is based on a method known as maximum a posteriori (MAP) estimation that allows incorporating a prior model of volumetric emissivities to assist the limit-angle reconstructions. To demonstrate the feasibility of this technique, we conduct a proof-of-concept study based on the simulation of the dayside magnetosphere ion population using a magneto-hydrodynamic (MHD) model, simulate 2-D soft X-ray images using LEXI's orbit and attitude, implement a prior model of emissivities and perform the 3-D estimations based on the MAP theory. Additionally, we consider several realistic sources of uncertainty in the simulated images, such as Poisson-distributed shot noise, astrophysical background emission, and the inclusion of the point spread function of the optical system.

This paper is organized as follows. Section 2 describes the statistically-based technique to estimate volumetric emissivities from 2-D soft X-ray images, the quantitative indexes to measure estimation accuracy, and the methods to estimate the magnetopause location from retrieved 3-D emissivities. Section 3 presents a set of experiments designed to evaluate the feasibility of our proposed statistically-based estimation approach, as well as actual retrievals derived from synthetic measurements based on LEXI's orbit and attitude. Section 4 discusses the sources of error in the estimation. Finally, Section 5 summarizes the conclusions of this study.

2. Methods and Mission Data

2.1 Statistical Estimation of Magnetosheath Soft X-ray Emissivities

Our technique aims to estimate volumetric soft X-ray emissivities, P, which are generated by the solar wind charge exchange (SWCX) interaction between heavy ions and exospheric hydrogen atoms and can be expressed as:

$$P = a n_H n_{sw} \langle g \rangle , \qquad (2)$$

where P is in $(eV\,cm^{-3}s^{-1})$, a is an efficiency factor expressed in units of $(eV\ cm^2)$ that depends on SWCX cross-section, SWCX photon energies, and the ratio between the concentration of solar wind heavy ions to the concentration of protons, n_H is the volumetric exospheric density in units of $(atoms\ cm^{-3})$, n_{sw} is the solar wind proton density in units of $(ions\ cm^{-3})$, and $\langle g \rangle = \sqrt{v_{sw}^2 + v_{th}^2}$ $(cm\ s^{-1})$ is the relative velocity of neutral and ions calculated with the plasma bulk speed v_{sw} and thermal speed v_{th} under the assumption of negligible neutral velocity (Sibeck et al., 2018; Walsh et al., 2016).

The photometric observation of P along a given line-of-sight (LOS) is represented by the following linear emission model:

$$I(\boldsymbol{r}, \hat{\boldsymbol{n}}, t) = \frac{1}{4\pi} \int_0^{L_{max}} P(\boldsymbol{r}, t)\mathrm{d}l + I_{bkg}(\hat{\boldsymbol{n}}, t) . \qquad (3)$$

Here, $I(\boldsymbol{r}, \hat{\boldsymbol{n}}, t)$ is the time-dependent soft X-ray energy flux (in units of $(eV\ cm^{-2}\ s^{-1}\ str^{-1})$) acquired by an observer located at a geocentric distance $\boldsymbol{r}$ with LOS direction $\hat{\boldsymbol{n}}$ (See Figure 1). In this study, I represents the measurement from a single pixel of the LEXI imaging sensor. The term $P(\boldsymbol{r}, t)$ is assumed to have an isotropic emission pattern such that the factor 4π can effectively extract the LOS flux. Also, the line-integral is properly evaluated along the LOS from the spacecraft position ($l = 0$) up to an appropriate outer boundary of the solution domain ($l = L_{max}$). The term $I_{bkg}(\hat{\boldsymbol{n}}, t)$ represents the astrophysical soft X-ray background emission along the LOS direction $\hat{\boldsymbol{n}}$ that can be extracted from models or alte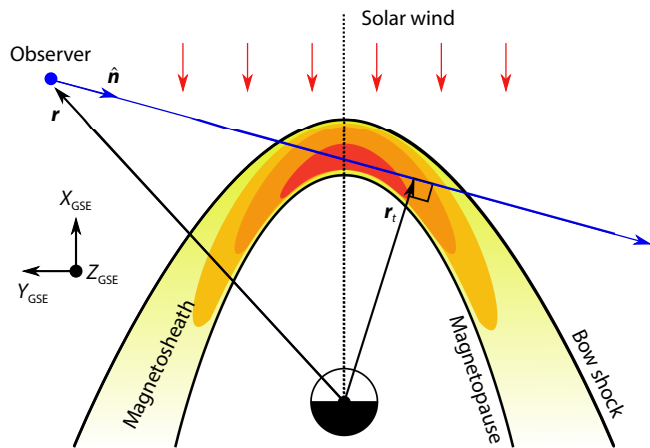rnative observations (e.g., ROSAT, XMM-Newton, Chandra X-ray Observatory). Figure 1 shows a two-dimensional scheme for magnetosheath observation in soft X-rays. The blue line represents the observer's LOS, while the yellow-to-red region represents the magnetosheath soft X-ray emissivity, P.

The proposed estimation technique is an example of inverse methods and relies heavily on the linearity between (i) the 3-D physical property of a given target and (ii) the intensity of its remote sensing observations. The emission model presented in Equation (3) provides the necessary conditions to retrieve volumetric soft X-ray emissivities of the dayside magnetosphere. In this study, we follow the steps presented in Cucho-Padin et al. (2022) in the context of exospheric tomography to formulate and solve a soft X-ray inverse problem.

First, we define the solution domain as a 3-D spherical region and discretize it into uniform spherical voxels, assuming that the volumetric emissivity is constant within each voxel boundary. The voxel size is defined by its radial Δr, azimuthal $\Delta\phi$, and polar $\Delta\theta$ distances. Also, we define N as the total number of voxels in the solution domain.

Second, Equation (3) is also discretized, resulting in a compact algebraic linear system:

$$\boldsymbol{y} = \boldsymbol{Lx} \qquad (4)$$

where $\boldsymbol{y}$ is a $[M \times 1]$ vector of background-free measurements (i.e., the mth element of $\boldsymbol{y}$ is $y_m = I - I_{bkg}$), $\boldsymbol{x}$ is a $[N \times 1]$ vector of unknown emissivities corresponding to all the spherical voxels in the solution domain, and $\boldsymbol{L}$ is the $[M \times N]$ observation matrix derived from previous knowledge of measurement's LOS directions $\hat{\boldsymbol{n}}$, spacecraft locations, and voxel size (see details in Cucho-Padin et al. (2022)).

Third, to solve the system presented in Equation (4), we adopt a statistical Bayesian approach which considers a priori information of the physical target (i.e., volumetric emissivities) to avoid the sensitivity to observation noise (Nakano et al., 2014). In this method, the components of the linear system are assumed to be random variables hereafter denoted as $\boldsymbol{X}$ (emissivities) and $\boldsymbol{Y}$ (intensities). The solution to a Bayesian inverse problem is the posterior probability function which is calculated based on Bayes's theorem as follows:

$$p_{post}(\boldsymbol{X}|\boldsymbol{Y}) = \frac{p(\boldsymbol{Y}|\boldsymbol{X})p_{pr}(\boldsymbol{X})}{p(\boldsymbol{Y})} \propto p(\boldsymbol{Y}|\boldsymbol{X})p_{pr}(\boldsymbol{X}) , \qquad (5)$$

where term $\propto$ indicates proportionality, p defines a probability function with subscript "post" for posterior and "pr" for prior, and $p(\boldsymbol{Y}|\boldsymbol{X})$ is the probability function for a conditional distribution of $\boldsymbol{Y}$ when $\boldsymbol{X}$ is given, and it is associated with the form $\boldsymbol{Y} = \boldsymbol{LX}$. In this study, we assume that both $p_{pr}(\boldsymbol{X})$ and $p(\boldsymbol{Y}|\boldsymbol{X})$ are Gaussian-distributed. Thus, we define $\boldsymbol{X}_{pr}$ as a Gaussian random vector of the prior knowledge of the volume emissivities, which is comprised of a $[N \times 1]$ mean vector $\bar{\boldsymbol{x}}_{pr}$ and a $[N \times N]$ covariance matrix $\boldsymbol{\Sigma}_{pr}$. Similarly, we define $\boldsymbol{Y}$ as a Gaussian random vector of background-free soft X-ray measurements comprised of a $[M \times 1]$ mean vector $\bar{\boldsymbol{y}}$, and a $[M \times M]$ covariance matrix $\boldsymbol{\Sigma}_y$. Using this terminology, $p_{post}(\boldsymbol{X}|\boldsymbol{Y})$ can be expressed as follows (Aster et al., 2013):

Figure 1. Two-dimensional scheme of dayside magnetosphere observations in soft X-ray from a space-based platform located at $\boldsymbol{r}$ geocentric distance. Red shading region indicates peak emissivities in soft X-rays.

$$p_{post}(X|Y) \propto \exp\left(-\frac{1}{2}\left((\bar{y}-LX)^T\Sigma_y^{-1}(\bar{y}-LX)+(X-x_{pr})^T\Sigma_{pr}^{-1}(X-x_{pr})\right)\right). \quad (6)$$

When an appropriate prior X_{pr} is selected, the estimation of the desired posterior distribution $\hat{x}_{post}$ can be obtained by minimizing $-\ln(p_{post}(X|Y))$, which is also known as the Maximum a posteriori (MAP) estimation (see (Karl, 2005) for further details). Using the Sherman–Morrison–Woodbury formulation (Sherman and Morrison, 1950), the MAP estimation is expressed as:

$$\hat{x}_{MAP} = x_{pr} + \Sigma_{pr}L^T(L\Sigma_{pr}L^T + \Sigma_y)^{-1}(\bar{y} - Lx_{pr}). \quad (7)$$

Fourth, to generate the covariance matrix of measurement, Σ_y, we assume that soft X-ray observations are mainly contaminated by Poisson-distributed shot noise. This condition establishes a discrete Poisson-distributed probability function for Y that disagrees with our previous assumption of Gaussian-distributed functions for all variables. To overcome this issue, we use a particular property of a Poisson-distributed random variable in which the mean and the variance are identical. Then, we can approximate a Poisson-distributed to a Gaussian-distributed function following $P_{oiss}(\lambda) \approx \mathcal{N}(\lambda, \lambda)$, where the term $\mathcal{N}(\mu, \sigma^2)$ represents a Gaussian-distributed random variable with mean μ and variance σ^2, and the parameter λ is the mean of a Poisson-distributed random variable. This approximation obeys the Central Limit Theorem, which establishes that adding identical and independently distributed random variables will approximate a Gaussian distribution (Feller, 1968; Hajek, 2015). For example, the addition of ten Poisson-distributed probability functions with $\lambda = 1$ yields

$$P_{oiss}(\lambda = 1) + \cdots + P_{oiss}(\lambda = 1) = P_{oiss}(\lambda = 10) \approx \mathcal{N}(\lambda = 10, \lambda = 10).$$

Also, to quantify the effectiveness of this approximation, the Berry-Esseen theorem (Tyurin, 2009) recommends evaluating the maximum difference between the cumulative density functions (CDF) of the two random variables. Hence, we (i) calculated the probability density function (PDF) for both Gaussian and Poisson distributions using $\mu = \sigma^2 = \lambda \in [1, 20]$ (there are 20 different cases, and the value of λ represent the number of counts in the imaging sensor), (ii) calculated the CDF from the PDF, (iii) subtracted the Gaussian CDF from the Poisson CDF for each case, and (iv) identified the maximum absolute difference. Since the maximum difference could be at most 1 as we are working in the probabilistic domain, we can straightforwardly convert the "error in CDF difference" (e_{CDF}) into a percentage. With this procedure, we found that (e_{CDF}) decreases exponentially when λ increases. Also, for a $\lambda > 7$ the $e_{CDF} < 10\%$, which indicates that for a process with mean counts greater than 7, the approximation error is smaller than 10%. Once established the theory, we construct the covariance matrix of measurements, Σ_y, as a diagonal matrix whose (m, m) element is given by the mth element of the vector $\bar{y}$ such that $\Sigma_y = \text{diag}(\bar{y})$. For this, we assume that each observation y_m, converted into counts, is the mean of a Poisson-distributed random variable with parameter

$$\lambda = \text{round}(y_m \times S \times t_{int}),$$

where S is the sensor responsivity in units of (counts cm^2 str eV^{-1}), t_{int} is the integration time in units of seconds, and the function round discretize its argument. The value $S \times t_{int}$ is used to generate the discrete λ and them is divided from the resulting λ

to fix the units of Σ_y (see a similar procedure in the context of solar corona tomography in Butala et al. (2010)). Values of S and t_{int} for our specific application are provided later in the manuscript. We acknowledge that some of the pixels will not produce more than 7 counts and their deviation from a Gaussian distribution would be high. The simulations presented here also serve as a means to evaluate these assumptions, present their drawbacks and propose additional investigation for improvement.

Finally, to construct the covariance matrix of the prior model, Σ_{pr}, we use the Gaussian Random Markov Field (GRMF) approach closely following the steps described by Cucho-Padin et al. (2022) in the context of exospheric tomography. Through this method, Σ_{pr} provides an adequate spatial distribution of variance based on a priori information and imposes smoothness in the 3-D estimations.

For the sake of clarification, the proposed technique attempts to perform 3-D estimation with a limited number of images (as explained in Section 3). It implies that the ensemble of LOSs from the imaging sensor used in the estimation are almost parallel and thus do not provide 3-D information as expected in a model-free tomographic approach. The proposed technique heavily relies on the prior model to obtain an initial 3-D spatial structure of soft X-ray emitters within the solution domain, which is statistically modified by the input radiance data via MAP estimation. Furthermore, the covariance matrix provides the connectivity among voxels that supports the generation of physical values in the results. A similar MAP approach without a prior model will result in the minimum norm solution, which may yield negative values for emitter densities along a given LOS. Finally, the literature shows evidence of the reliability of this methodology in other space science applications, such as the 3-D estimation of the terrestrial exospheric density derived from a Far Ultraviolet single-image (Cucho-Padin et al., 2022) and the estimation of the terrestrial plasmaspheric He$^+$ density derived from an Extreme Ultraviolet single-image (Nakano et al., 2014). This work presents the use of this technique on magnetosheath estimation for the first time.

2.2 Methods to Estimate Magnetopause Location from Soft X-ray Emissivities

This section presents two methods to estimate magnetopause location from an ensemble of volume emissivity distributions along the Sun–Earth line denoted as $P_{SE}(r)$ where r is the geocentric distance ranging from 6 to 16 R_E.

In method 1, we first locate the peak value of the emissivity and its location along the Sun–Earth line using $P_{peak} = \max(P_{SE}(r))$ and $r_{max} = \text{argmax}(P_{SE}(r))$. Then, it is assumed that in the magnetopause location, r_{MP}, the emissivity is reduced to 10% of the peak value such that $10\% \times P_{peak} = P_{SE}(r_{MP})$. This relationship can be used to find r_{MP} considering that $6 R_E < r_{MP} < r_{max}$. The threshold value of 10% has been selected based on the previous analysis of soft X-ray emissivities at the magnetosheath and magnetopause using MHD models under different solar wind conditions.

In method 2, we first calculate the spatial derivative of the emissivity along the Sun–Earth line, i.e., $\nabla P_{SE}(r) = d(P_{SE}(r))/dr$. Then, it is assumed that the magnetopause location, r_{MP}, maximizes this

spatial derivative such that $r_{MP} = \text{argmax}(\nabla P_{SE}(r))$.

2.3 Assessment of 3-D Estimations

To evaluate the confidence of our 3-D estimations, we use the Root Mean Squared Error (RMSE) and the Structural SIMilarity index (SSIM). The RMSE is defined by

$$\text{RMSE} = \sqrt{\frac{\sum_{i=1}^{N}(\boldsymbol{x}_{GT_i} - \hat{\boldsymbol{x}}_{MAP_i})^2}{N}}, \tag{8}$$

where $\boldsymbol{x}_{GT}$ is the ground truth vector of volumetric emissivities, $\hat{\boldsymbol{x}}_{MAP}$ is the MAP estimate, subindex i indicates the ith element in the vectors, and N is the total number of voxels in the solution domain.

The SSIM index is defined as:

$$\text{SSIM} = \frac{(2\mu_{\boldsymbol{x}_{GT}}\mu_{\hat{\boldsymbol{x}}_{MAP}} + C_1)(2\sigma_{\boldsymbol{x}_{GT}\hat{\boldsymbol{x}}_{MAP}} + C_2)}{(\mu_{\boldsymbol{x}_{GT}}^2 + \mu_{\hat{\boldsymbol{x}}_{MAP}}^2 + C_1)(\sigma_{\boldsymbol{x}_{GT}}^2 + \sigma_{\hat{\boldsymbol{x}}_{MAP}}^2 + C_2)}, \tag{9}$$

where $\mu_{\boldsymbol{x}_{GT}}$ and $\sigma_{\boldsymbol{x}_{GT}}^2$ represent the mean and variance of $\boldsymbol{x}_{GT}$, $\mu_{\hat{\boldsymbol{x}}_{MAP}}$ and $\sigma_{\hat{\boldsymbol{x}}_{MAP}}^2$ indicate the mean and variance of $\hat{\boldsymbol{x}}_{MAP}$, and $\sigma_{\boldsymbol{x}_{GT}\hat{\boldsymbol{x}}_{MAP}}$ denotes the covariance between $\boldsymbol{x}_{GT}$ and $\hat{\boldsymbol{x}}_{MAP}$. Also, $C_1 = (K_1 L)^2$ and $C_2 = (K_2 L)^2$ are constant values where L is assigned with the maximum value in the dataset, and $K_1 = 0.01$ and $K_2 = 0.03$ as suggested by Wang RC et al. (2023) in a similar 3-D reconstruction context.

2.4 The Lunar Environment Heliospheric X-ray Imager (LEXI) Mission

The NASA Lunar Environment Heliospheric X-ray Imager (LEXI) instrument is a wide field-of-view (FOV) soft X-ray (0.1–2 keV) imager built to observe the interaction between the solar wind and the terrestrial magnetosphere over multiple days. LEXI will land on the lunar surface as part of NASA's Commercial Lunar Payload Services program and will measure soft X-ray emissions with its $9.1° \times 9.1°$ FOV using a tiled 3 by 3 array of "lobster-eye" micropore optics (Paw et al., 2022). Operating from the lunar surface, LEXI will be in the lunar orbit, which is nearly circular with a geocentric radius of $\approx 60\ R_E$, a 28-day period, and 5.145° inclination to the ecliptic plane. The payload is actively pointed with a gimbal to maintain pointing at the dayside magnetosheath as the moon orbits Earth.

3. Estimation of the Magnetosheath Region

3.1 Experiment Settings

In this section, we describe the variables and the set of experiments needed to demonstrate the feasibility of the proposed technique in estimating the magnetosheath emissivity structure from simulated soft X-ray images of the LEXI mission.

First, we calculate the ground truth emissivity vector of the magnetosheath, $\boldsymbol{x}_{GT}$, which is used to generate synthetic soft X-ray measurements. To do so, we use the magneto-hydrodynamic (MHD) model Open Geospace General Circulation Model (OpenGGCM) (Raeder et al., 2001, 2008) to generate the proton density distribution (n_{sw}) in the dayside magnetosheath. The boundaries of this region in Geocentric Solar Ecliptic (GSE) coordinates are

$X_{GSE} \in [0, 16]\ R_E$, $Y_{GSE} \in [-20, 20]\ R_E$, and $Z_{GSE} \in [-5, 5]\ R_E$, with a spatial resolution of $0.1\ R_E$. This rectangular region is hereinafter referred to as the "rectangular grid". For this proof-of-concept study, we ran OpenGGCM with the following conditions: solar wind density $n_{sw} = 21.25$ cm^{-3}, velocity $v_x = 400$ km s^{-1}, $v_y = v_z = 0$, ion temperature $T_i = 10^5$ K and interplanetary magnetic field (IMF) $B_x = 2$ nT, $B_y = 2$ nT, $B_z = -4$ nT, i.e. for a solar wind plasma much denser than typically observed. For the neutral density distributions (n_H), we consider a spherically symmetric exosphere that follows the form Connor and Carter (2019):

$$n_H(r) = n_0 \left(\frac{10R_E}{r}\right)^3, \tag{10}$$

where n_H is in (atoms cm^{-3}), n_0 is the atomic hydrogen density at the $10\ R_E$ subsolar point with a value of 25 (atoms cm^{-3}), and r indicates the geocentric distance in units of R_E. Also, we adopt an efficiency factor equal to $\alpha = 1 \times 10^{-15}$ (eV cm^2) (Jorgensen et al., 2019b). Then, the volume emissivity rate, P, can be calculated using Equation (2). Note that in this research work, we focused on the 3-D estimation of an assumed static magnetosheath, i.e., neither the bow shock nor the magnetopause moves during data collection periods. In addition, we identified and extracted the inner magnetospheric region from our MHD simulation since it does not contain sufficient heavy solar wind ions and, therefore, will not produce soft X-ray emissivities. For this task, we used the method described by Samsonov et al. (2022a), which determines the inner magnetosphere according to the following equations:

$$\begin{aligned} p &< p(\text{msp}) + \Delta p, \\ V_x &> V_x(\text{sw}) \times k_v, \end{aligned} \tag{11}$$

where $p(\text{msp})$ is the typical thermal pressure of the magnetospheric region, $V_x(\text{sw})$ is the solar wind velocity in the x axis, and the terms ΔP and k_v are used to adjust the comparison. Using information from our MHD, we found that $p(\text{msp}) \approx\ < 0.1$ and $V_x(\text{sw}) = -400$ (km s^{-1}). Also, we assume $\Delta P = 0.2$ nT and $k_v = 0.15$, as recommended in Samsonov et al. (2022a). Then, when both conditions in Equation (11) match, the location is considered part of the inner magnetosphere and a mask is created to filter this region.

Second, we adopted a spherical sector as the region of interest (ROI) where the estimation will be performed. Table 1 shows the dimensions of the ROI, which considers: (i) sufficient volumetric coverage where most of the magnetosheath soft X-ray emissivity is expected, and (ii) the observational coverage imposed by the simulated LEXI viewing geometry, e.g., LEXI cannot observe emissivities beyond $\theta = \pm 35°$ due to its FOV. Following the proposed methodology for 3-D estimation, the ROI is divided into spherical voxels with dimensions provided in the third column of Table 1. The selection of voxel resolution is based on a Fourier-based analysis of the spatial distribution of magnetosheath emissivities, which resulted in a set of dimensions that guarantee the capture of spatial gradients (i.e., emissivity variation in a given distance) in the 3D structure. Figure 2 shows the spherical ROI in the GSE coordinate system (hereinafter referred to as the "spherical grid"), which is the solution domain for the estimation, $\hat{\boldsymbol{x}}_{MAP}$.

Third, to calculate the prior model of the magnetosheath emissivi-

Table 1. Dimension and ranges of the Region of Interest (ROI).

ROI dimension	Range	Voxel dimension
Radial (r)	[6−16] R_E	0.1 R_E
Azimuthal (ϕ)	[−90, 90] degrees	10 degrees
Polar (θ)	[−35, 35] degrees	5 degrees

ties, x_{pr}, we first used Shue et al. (1998) and Jelínek et al. (2012) models to identify the boundaries of the magnetopause and bow shock, respectively, based on the solar wind conditions previously used to generate the ground truth. Then, we fill out the magnetosheath and outer bow shock region with soft X-ray emitters using the parametric formulation (Equation 8 in the reference) and identical coefficients ($A_1 = 3.2285 \times 10^{-5}$ eV cm^{-3} s^{-1}, $B = -1.7985 \times 10^5$ eV cm^{-3} s^{-1}, $\alpha = 2.4908$, $\beta = -1.6458$, $A_2 = 1.3588 \times 10^{-5}$ eV cm^{-3} s^{-1}) described in Jorgensen et al., (2019a) as a first approximation. Note that our goal is to demonstrate that even with a prior model significantly different from the ground truth, we can still estimate the structure from soft X-ray observations with a given degree of uncertainty. Also, we characterize this prior model using the SSIM index calculated with respect to the ground truth, SSIM = 0.3.
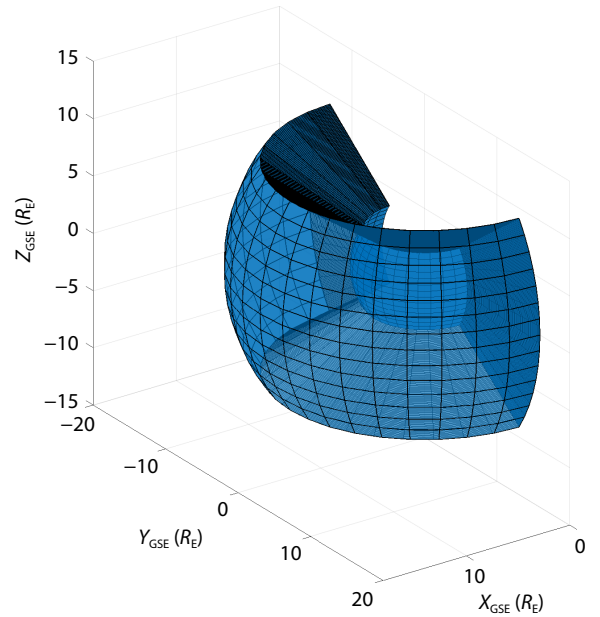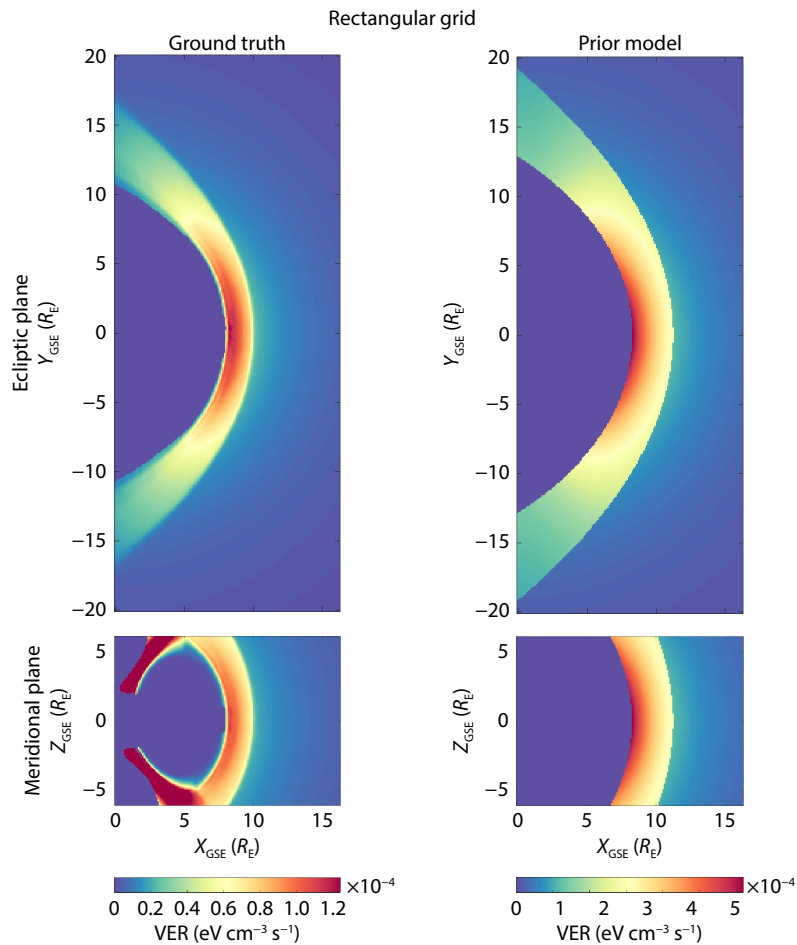

Figure 2. Region of interest (ROI) used as the solution domain of the estimation approach. ROI dimensions and voxel size are specified in Table 1.

Figure 3. The ground truth and the prior model of soft X-ray emissivities in rectangular shown in the rectangular coordinate system. The top panels show the ecliptic planes ($\theta = 0°$), and the bottom panels show the meridional planes ($\phi = 0°$). All plots use the Geocentric Solar Ecliptic (GSE) coordinate system. VER = volume emission rate.

Gonzalo CP et al.: Finding the magnetopause location using soft X-ray observations and a statistical inverse method

Figure 3 shows the ground truth and prior soft X-ray emissivities (also referred to as volumetric emission rate or VER) using the high-resolution rectangular grid. The top row shows the ecliptic planes ($\theta = 0°$), while the bottom panel shows the meridional planes ($\phi = 0°$). With a similar format, Figure 4 shows the corresponding soft X-ray emissivities using the spherical grid. Emissivity values in the spherical grid (x_{GT}^S, x_{pr}^S) have been obtained by linear interpolation of those from the rectangular grid (x_{GT}^R, x_{pr}^R). In this study, the vector x_{GT}^R is used to generate synthetic soft X-ray measurements, the vector x_{pr}^S is used as the prior model in the MAP estimation, and the vector x_{GT}^S is used to assess 3-D estimations. It is noteworthy that the prior model is significantly different from the ground truth in both structure and absolute emissivity values, a condition that serves to investigate realistic scenarios wherein the

physics included in the prior are insufficient to describe the real magnetosheath ion density distribution.

Fourth, for this study, we assume that the LEXI instrument is in a circular orbit with no inclination, i.e., within the ecliptic plane. Also, we consider that LEXI starts observing the dayside magnetosphere when it is located at an azimuthal angle $\phi_I = 39°$ and acquires images during ≈ 6 days until it reaches an azimuthal angle $\phi_F = 117°$. During these days, the LEXI's viewing geometry is considered constant and points toward $[8.5, 0, 0]$ R_E. Figure 5 shows an observation scheme for the LEXI instrument. The blue region represents the spherical grid where the 3-D estimation is carried out, the red dots indicate several Lunar positions from where LEXI acquires images, and the green regions represent the LEXI's FOV of $9.1° \times 9.1°$ projected to the ecliptic plane. In addition,
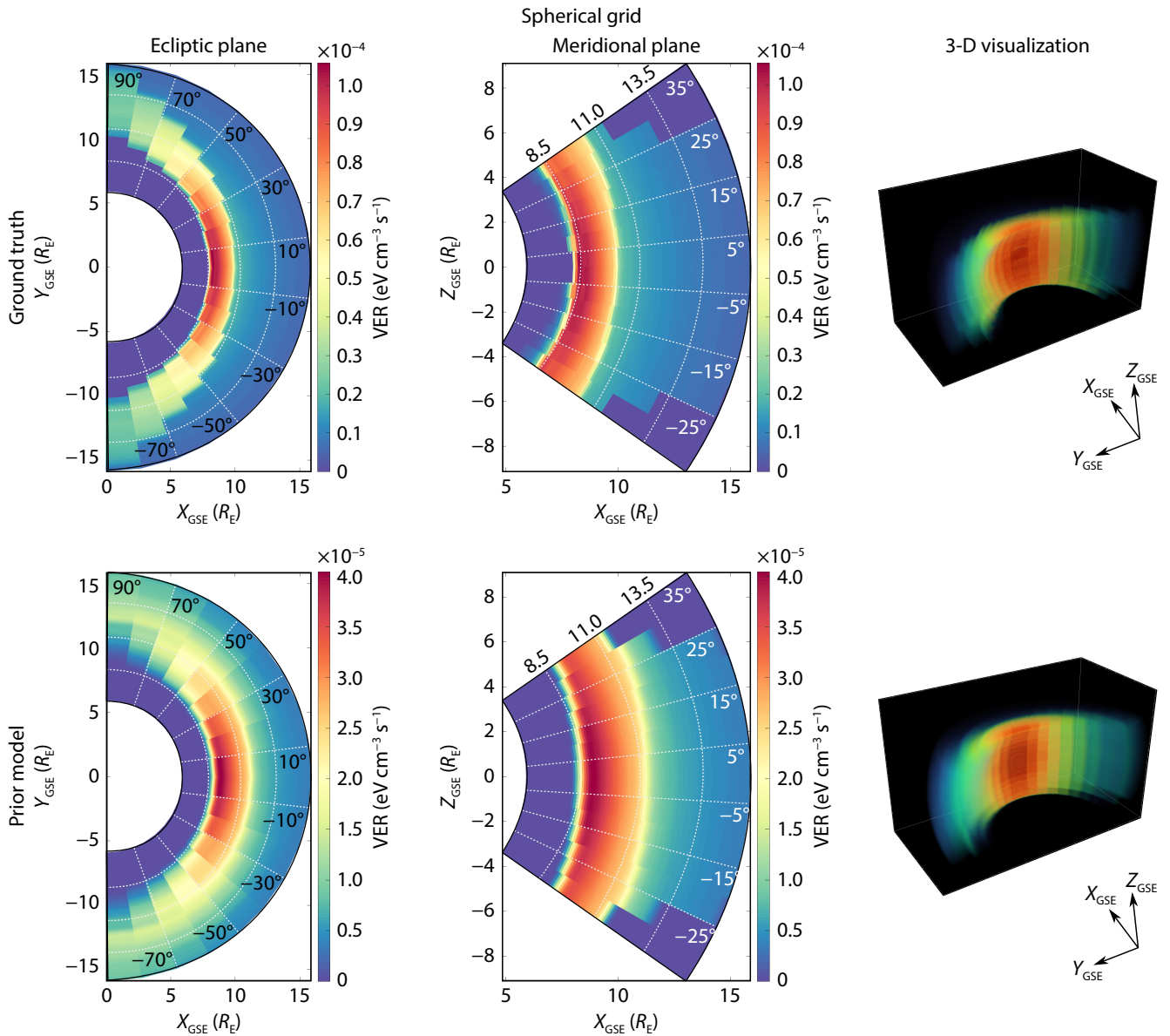

Figure 4. The ground truth and prior model of soft X-ray emissivities shown in the spherical coordinate system. The top row shows the ecliptic and meridional planes and a 3-D visualization of the ground truth emissivities. Similarly, the bottom row shows the ecliptic and meridional planes and a 3-D visualization of the prior model of emissivities. All plots use the Geocentric Solar Ecliptic (GSE) coordinate system. VER = volume emission rate.
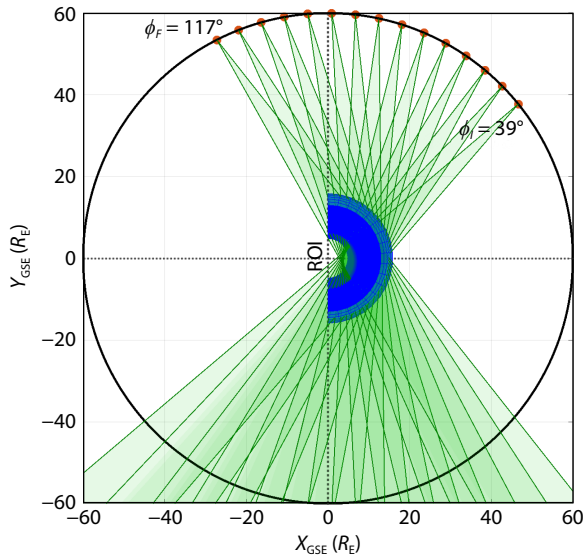
Figure 5. Scheme for LEXI observations of the dayside magnetosphere. Red dots indicate several LEXI locations around the circular orbit, green regions are the LEXI's FOV projected into the XY_{GSE} plane, and the blue region is the spherical solution domain of the proposed approach. Observations start when LEXI is at $\phi_i = 39°$ and last for ~6 days when LEXI is at $\phi_F = 117°$.

to create a LEXI image, we assume an integration time, t_{int} of 10 minutes, as well as a pixel resolution of $R_{px} = 0.25$ (degrees/pixel), which yields a square image of 37×37 pixels.

Finally, we define a set of experiments for 3-D estimations that consider eight (8) different locations for the LEXI instrument that are uniformly distributed within the 6-day acquisition period and

Table 2. List of experiments implemented in this study to evaluate technical feasibility.

| Experiment number	Initial angle (ϕ_i) (degrees)	Final angle (ϕ_f) (degrees)	Number of images
1	39.00	39.08	2
2	39.00	39.24	4
3	39.00	39.40	6
4	48.70	48.78	2
5	48.70	48.94	4
6	48.70	49.10	6
7	58.50	58.58	2
8	58.50	58.74	4
9	58.50	58.90	6
10	68.20	68.28	2
11	68.20	68.44	4
12	68.20	68.60	6
13	78.00	78.08	2
14	78.00	78.24	4
15	78.00	78.40	6
16	87.70	87.78	2
17	87.70	87.94	4
18	87.70	88.10	6
19	97.50	97.58	2
20	97.50	97.74	4
21	97.50	97.90	6
22	107.20	107.28	2
23	107.20	107.44	4
24	107.20	107.60	6
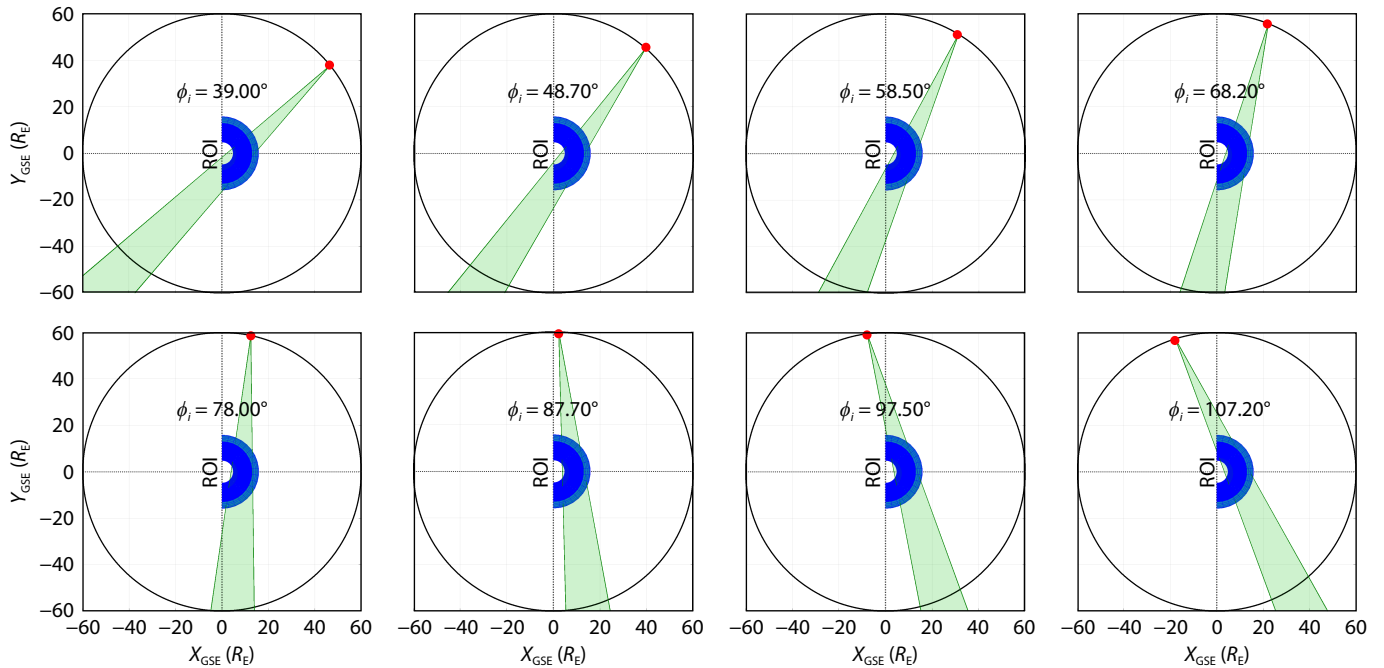
Figure 6. Scheme for each of the eight (8) initial angles (ϕ_i) of the LEXI platform considered in the list of experiments. The red dot indicates the LEXI's location, the green region represents LEXI's FOV, and the blue region is the spherical solution domain utilized in the proposed methodology.

Gonzalo CP et al.: Finding the magnetopause location using soft X-ray observations and a statistical inverse method

three (3) different numbers of images used in the inversion method. Table 2 lists these experiments and indicates the azimuthal angles where acquisition starts and ends (denoted as ϕ_i and ϕ_f, respectively) and the number of images to be used in each estimation process. The distance between the acquisition of two images is identical to the integration time of 10 minutes, corresponding to an angular displacement of $\approx 0.08°$ along the orbit. Figure 6 shows the initial location of the LEXI instrument for each experiment.

3.2 Magnetosheath Estimation from Synthetic Soft X-ray Images

Our study of 3-D estimations of the magnetosheath requires the generation of synthetic soft X-ray images for each experiment in Table 2. To do so, we first build the observation matrix $\boldsymbol{L}$ using the information on (i) the LEXI instrument position, (ii) the line-of-sight (LOS) direction ($\hat{\boldsymbol{n}}$) of each of the 37×37 pixels per image,

and (iii) the size of the spherical voxels. We calculate the intersection of the LOS with voxels in the solution domain, and the lengths of the resulting line sectors are used to populate the matrix $\boldsymbol{L}$ (see Cucho-Padin et al. (2022) for details). Then, the "ideal" synthetic soft X-ray measurements can be calculated using the formula $\boldsymbol{y} = \boldsymbol{L}\,\boldsymbol{x}_{GT}^{R}$. Figure 7a shows an example of a synthetic image in units of energy flux. We use the ground truth emissivity vector in the rectangular grid, $\boldsymbol{x}_{GT}^{R}$, to assess how the sampling process to a spherical grid can affect the estimations.

Also, we consider three optical processes that modify the ideal synthetic measurements: the astrophysical soft X-ray background emission, the point spread function (PSF) of the optical system, and the Poisson-distributed shot noise. To include them in one image, we follow the next steps: (i) Calculate the number of counts per pixel using the imaging sensor responsivity S (counts cm^2 str deg^{-2} eV^{-1}) and the LEXI's optics/filter performance ratio F (unit-less) in the formula $\boldsymbol{y}_c = \boldsymbol{y} \times S \times R_{px}^2 \times t_{int} \times F$
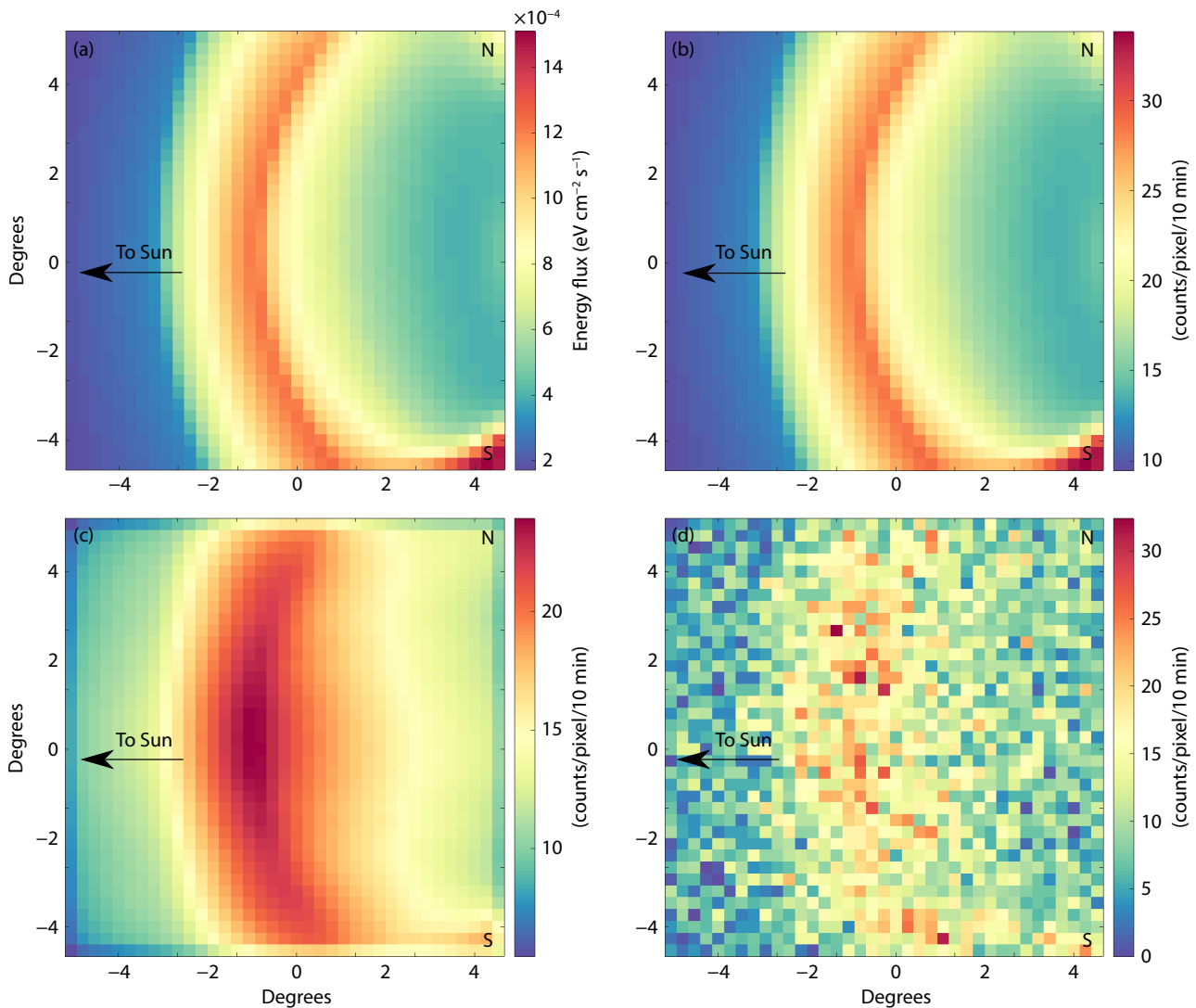

Figure 7. Panel a shows the "ideal" synthetic measurements in units of energy flux obtained using the LEXI's FOV and the ground truth soft X-ray emissivity in the rectangular grid ($\boldsymbol{x}_{GT}^{R}$). Panel b shows the measurements in counts per pixel per 10 minutes integration time added with the astrophysical background ($\boldsymbol{y}_{c+I_{bkg}}$), panel c shows the convolution of the previous result with the PSF of the LEXI's instrument ($\boldsymbol{y}'_{c+I_{bkg}+PSF}$), and panel d shows the addition of Poisson-distributed noise to the image ($\boldsymbol{y}'_N$), which is also referred to as the "realistic" measurement.

(see an example of a resulting image in Figure 7b), (ii) add the astrophysical background emission I_{bkg} (counts deg^{-2} s^{-1}) using $\mathbf{y}_{c+I_{bkg}} = \mathbf{y}_c + I_{bkg} \times R_{px}^2 \times t_{int} \times F$, (iii) include the PSF effect by arranging $\mathbf{y}_{c+I_{bkg}}$ into a 2D matrix with size 37×37 pixels to form an image and then apply the convolution with the PSF kernel, i.e., $\mathbf{y}'_{c+I_{bkg}+PSF} = \mathbf{y}'_{c+I_{bkg}} \circledast PSF$ where super index ι indicates the 2D distribution (see an example of results of steps (ii) and (iii) in Figure 7c), and (iv) include Poisson-distributed noise as follows $\mathbf{y}'_N = P_{oiss}(\mathbf{y}'_{c+I_{bkg}+PSF})$ (see an example in Figure 7d). Additional steps include rearranging the matrix into a column vector, performing previous steps for remaining images in the ensemble, and converting counts back into intensities using the sensor responsivity and performance ratio as needed by the proposed methodology. We refer to this processed data, $\mathbf{y}_N$, as the "realistic" synthetic measurements. Also, in this study, we used the following values for astrophysical background emission $I_{bkg} = 0.27$ (counts deg^{-2} s^{-1}), imaging sensor responsivity $S = 1.22 \times 10^{-6} \times 4\pi$ (counts cm^2 str deg^{-2} eV^{-1}), optics/filter performance ratio $F = 0.625$, and $t_{int} = 10$ (minutes), which were provided by the LEXI's science team via personal communication.

To understand how the optical processes can affect the retrievals, we conducted the proposed experiments using both ideal and realistic synthetic measurements. Figure 8 shows the 3-D estimation results for experiment 1 using ideal synthetic measurements. LEXI acquires two images starting at an angle $\phi_i = 39°$ with an integration time of 10 minutes per image. Panels a and b show the LOS density in the ecliptic and meridional planes, respectively, which serve to identify the actual coverage of the solution domain by the LEXI observations. White voxels indicate no coverage, while blue-to-yellow colors indicate the amount of LOSs passing through a given spherical voxel. Panels c and d show the 3-D estimations of soft X-ray emissivities in the ecliptic and meridional planes, respectively. Panel e shows a 3-D visualization of the 3-D estimation. To evaluate how these results serve to determine the magnetopause location, panel f shows the ground truth, the prior, and the estimated emissivities along the Sun–Earth line. Specifically, the red line with square markers shows estimated soft X-ray emissivities along the Sun–Earth line ranging from 6 to 16 R_E geocentric distance, the blue line with triangle markers shows the ground truth emissivity (obtained from $\mathbf{x}_{GT}^R$), and the black line with circle markers shows the emissivities of the prior model (obtained from $\mathbf{x}_{pr}^S$). Results in Panel f indicate that the proposed algorithm effectively uses the input data (soft X-ray measurements) to obtain estimates that significantly deviate from the prior model, especially in terms of emissivity amplitude. However, the spatial structure is still similar to that provided by the prior, a result associated with the lack of coverage. Further, panel c shows only a partial 3-D estimation of the magnetosheath since the FOV of both LEXI images used in this experiment mainly captures the pre-noon region of the magnetosheath.

With an identical format of Figure 8, Figure 9 shows the results of the 3-D estimation for experiment 16 using ideal synthetic measurements. In this case, LEXI acquires two images starting at an angle $\phi_i = 87.7°$ with an integration time of 10 minutes per image. Panel c shows a complete estimation of the magnetosheath structure (from pre to post-noon) associated with the coverage

achieved with the FOV of both LEXI images. Panel f shows that the estimated emissivity profile along the Sun–Earth line deviates significantly from the prior model and intends to be similar to the ground truth profile in both amplitude and structure. It demonstrates that assumptions used in our approach are sufficient to estimate emissivities from a limited number of images when a physics-based prior model is provided.

In order to assess our 3-D retrievals of emissivities, we calculated the RMSE and SSIM index for each of the 24 experiments. In both panels of Figure 10, the black diamonds indicate the values of RMSE (top panel) or SSIM (bottom panel) calculated using the 3-D ground truth emissivity ($\mathbf{x}_{GT}^S$) and the estimated emissivity ($\hat{\mathbf{x}}_{MAP}^S$), the green numbers at the top indicate the initial angle of the image acquisition (ϕ_i), the blue numbers below each diamond indicate the number of images used for each estimation, and the gray line indicates the RMSE/SSIM values calculated using emissivities of the prior model ($\mathbf{x}_{pr}^S$) and the ground truth ($\mathbf{x}_{GT}^S$). The results indicate that 3-D estimation of emissivities using images acquired from azimuthal angles $> \sim 50°$ provide the best combination for RMSE and SSIM indexes and significantly improve the results obtained with the prior model.

To evaluate the two methods that determine magnetopause location from 3-D estimations, we first define its real position as the point along the Sun–Earth line where the derivative of the proton density (obtained from the OpenGGCM model) is maximum, resulting in $r_{MP} = 8.05 R_E$. Then, for each 3-D estimation, we calculate the location of the magnetopause using method 1 (r_{MP}^1) and method 2 (r_{MP}^2). To facilitate the visualization, Figure 11 shows the error in the magnetopause location, defined as ($r_{MP} - r_{MP}^1$) for method 1 (top panel) and ($r_{MP} - r_{MP}^2$) for method 2 (bottom panel). Information in both panels is provided with the identical format used in Figure 10. In this case, the gray line indicates the error of the magnetopause location in the prior model with respect to r_{MP}. The results indicate that estimating magnetopause location heavily relies on the initial angle (ϕ_i) of the image acquisition. Further, the lowest values of the error in magnetopause location are found when $\phi_i > \sim 50$ for both methods. Also, the results suggest that magnetopause location based on method 1 provides better results than method 2 for the same range of ϕ_i.

The following figures show the results of 3-D estimations using "realistic" synthetic soft X-ray measurements. For this case, we conducted 50 iterations for each of the 24 experiments. In each iteration, the estimation process used a different set of images owing to the inclusion of the random Poisson-distributed shot noise. Figure 12 follows a similar format to Figure 8 and displays the results for experiment 1 using two realistic soft X-ray images acquired from the starting point at $\phi_i = 39°$. Panels c, d, and e estimate emissivities for one (1) iteration. In panel f, the red line with square markers displays the mean (μ) of the retrieved emissivity values along the Sun–Earth line for the 50 iterations, while the red-shaded region represents the corresponding standard deviation (σ) of those values. Similar to the results shown in Figure 8, panel c shows a partial 3-D estimation of the magnetosheath, while panel f shows that the retrieved emissivity values are much smaller than those in the ground truth. This feature is associated with the convolution with the PSF, which significantly reduces the

number of counts in the synthetic image; therefore, an underestimation of emissivities is expected.

With a similar format to Figure 12, Figure 13 shows 3-D estimations

for experiment 16, which uses two realistic soft X-ray images acquired from the starting point at $\phi_i = 87.7°$. Panels c, d, and e show the retrievals of emissivities for one (1) iteration, while panel e shows the retrievals of emissivities along the Sun−Earth line for
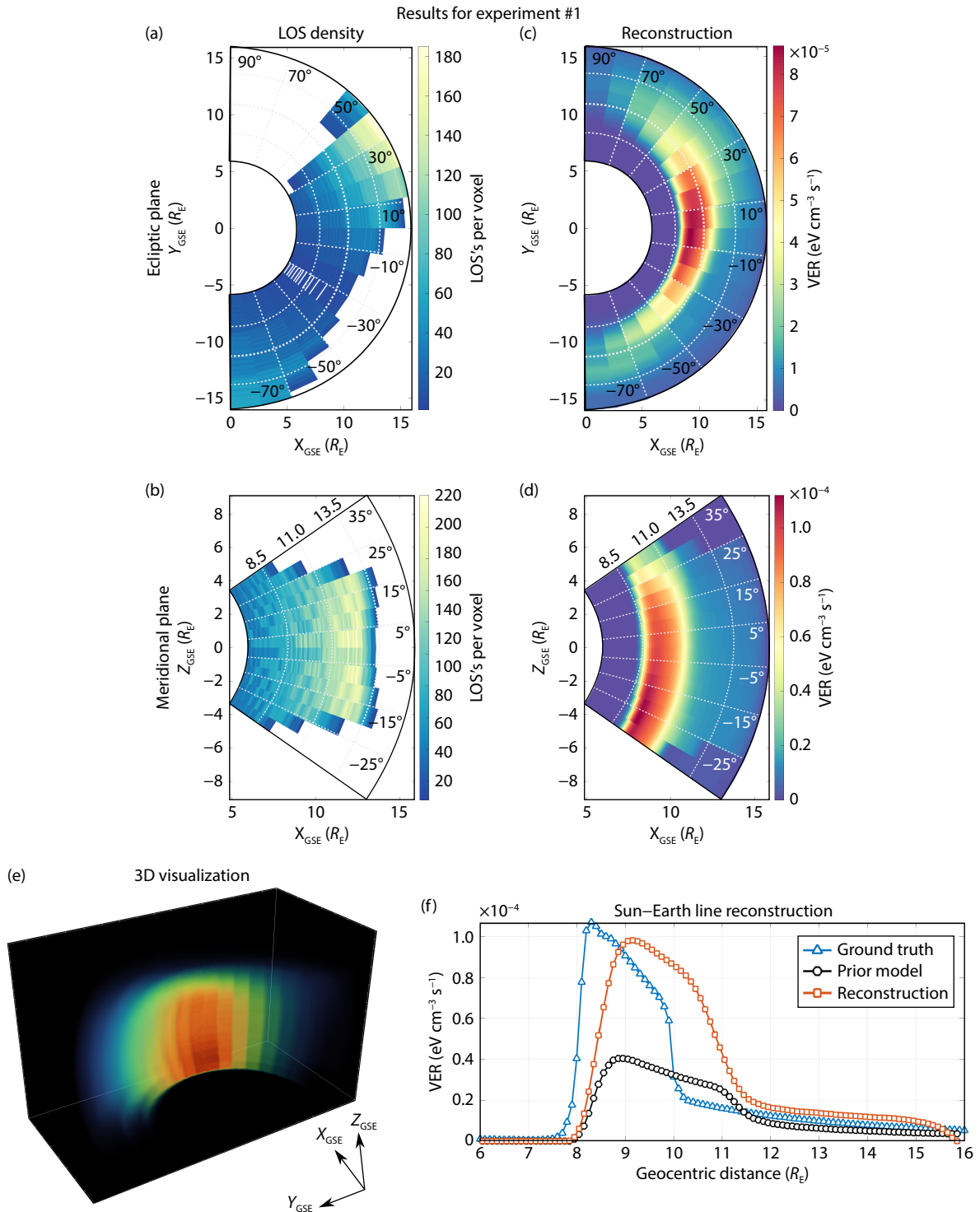

Figure 8.   Three-dimensional estimation of emissivities for experiment 1 using ideal soft X-ray measurements. Panels a and b display the meridional and ecliptic planes of LOS density per voxel, i.e., the number of LEXI's LOSs passing through a single voxel. Panels c, d, and e show the meridional and ecliptic planes and a 3-D visualization of estimated soft X-ray volumetric emissivities. Panel f depicts soft X-ray emissivities along the Sun−Earth line where the blue line indicates the ground truth, the black line displays the prior model, and the red line shows the estimation of emissivities using our proposed technique.

50 iterations. Similar to the results with ideal synthetic measurements, this location favors the complete estimation of the magnetosheath structure.

Figure 14 shows the values of RMSE (top panel) and SSIM index (bottom panel) for each experiment. The results of the 50 iterations per experiment were statistically processed to show box plots
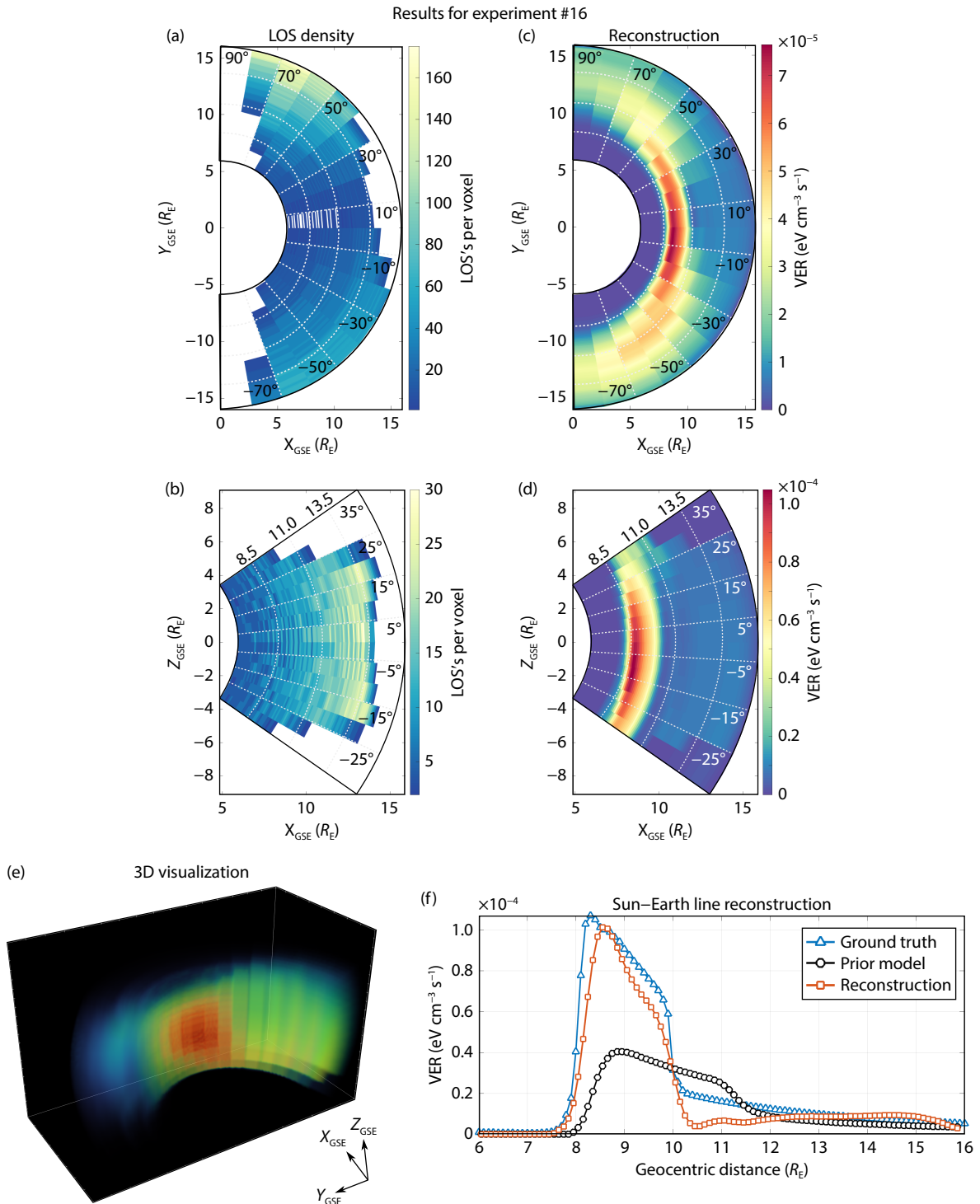

Figure 9. Three-dimensional estimation of emissivities for experiment 1 using ideal soft X-ray measurements. Panels a and b display the meridional and ecliptic planes of LOS density per voxel, respectively. Panels c, d, and e show the meridional and ecliptic planes and a 3-D visualization of estimated soft X-ray volumetric emissivities. Panel f depicts soft X-ray emissivities along the Sun−Earth line where the blue line indicates the ground truth, the black line displays the prior model, and the red line shows the estimated of emissivities using our proposed technique.
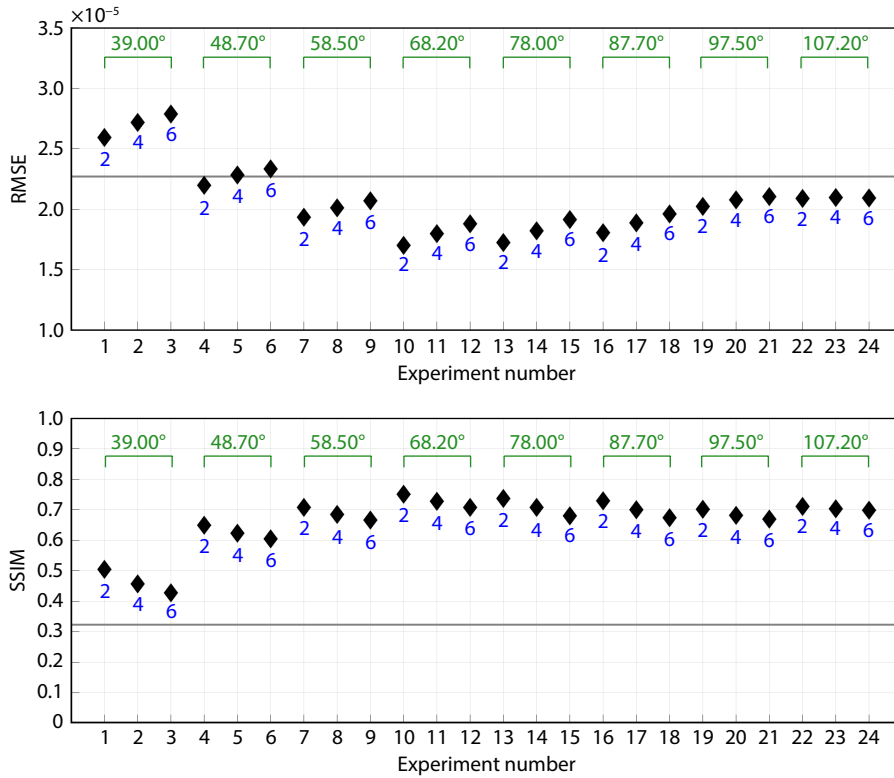
Gonzalo CP et al.: Finding the magnetopause location using soft X-ray observations and a statistical inverse method

Figure 10. RMSE (top panel) and SSIM (bottom panel) values for each experiment using "ideal" synthetic soft X-ray measurements. The green numbers indicate the initial angle (ϕ_i) for each experiment, and the blue numbers indicate the number of images used in the estimation process.
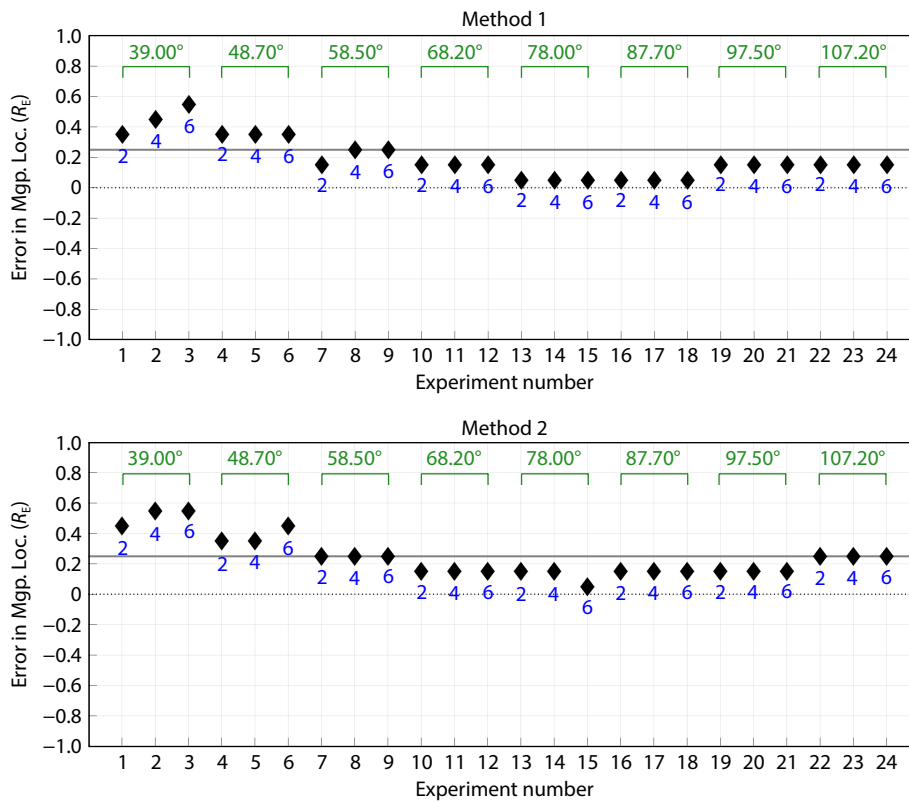

Figure 11. Error in magnetopause location derived from 3-D estimations. The green numbers indicate the initial angle (ϕ_i) for each experiment, and the blue numbers indicate the number of images used in the estimation process.

wherein the length of the blue box indicates the variability of the data, the vertical dashed black line displays the maximum and minimum values in the dataset, the red line within the box represents the median, the green diamond indicates the mean of the dataset, and red crosses represent data outliers. Also, the gray line indicates the RMSE or SSIM calculated using the prior model and the ground truth emissivity. The results show that experiments with $\phi_i > 78°$ produce low RMSE values and high SSIM indexes
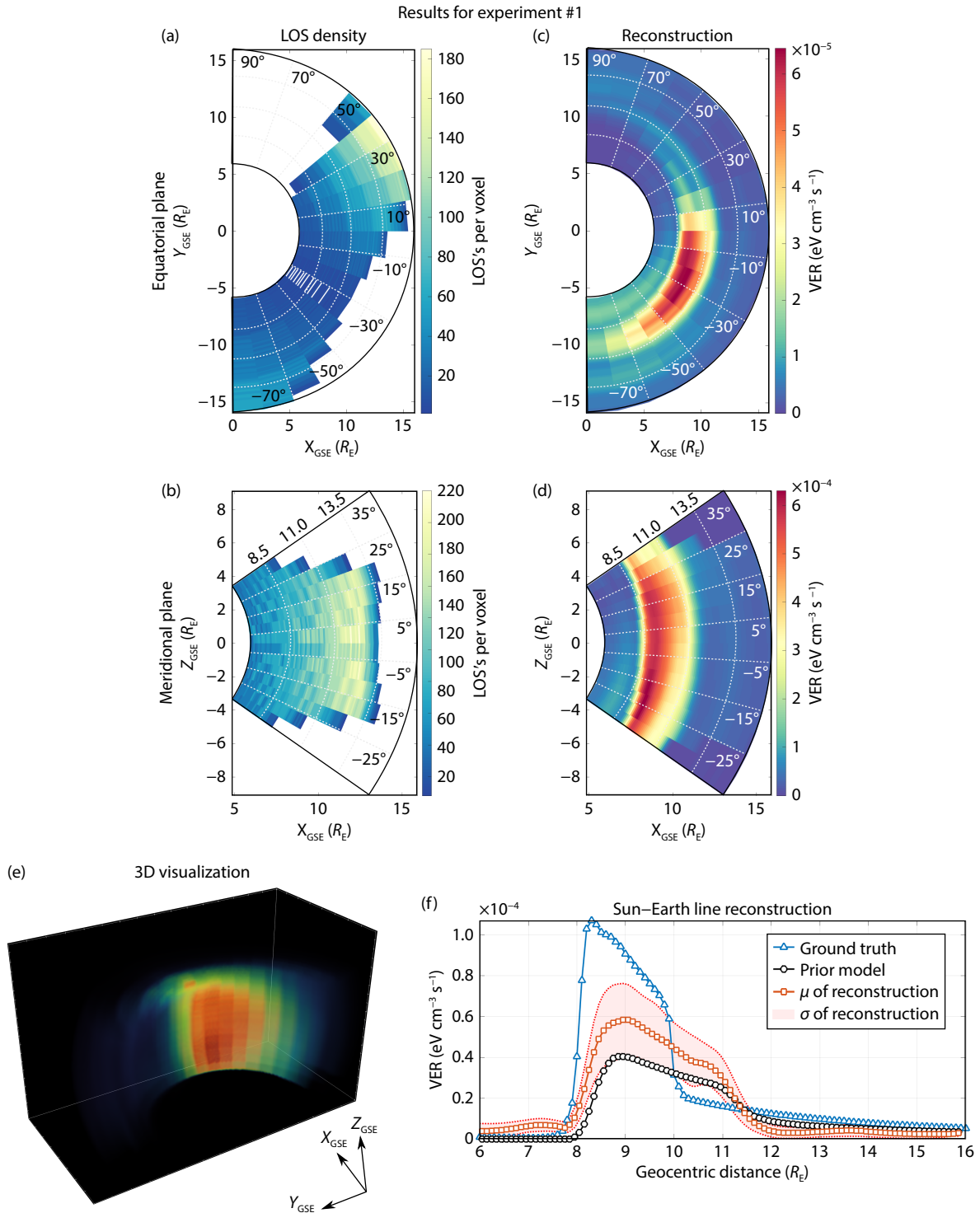

Figure 12. Three-dimensional estimation of emissivities for experiment 1 using realistic synthetic soft X-ray measurements. Panels a and b display the meridional and ecliptic planes of LOS density per voxel, respectively. Panels c, d and e show the meridional and ecliptic planes and a 3-D visualization of estimated soft X-ray volumetric emissivities. Panel f depicts soft X-ray emissivities along the Sun−Earth line where the blue line indicates the ground truth, the black line shows the prior model, and the red line and shadow region display the mean and standard deviation, respectively, of 50 estimations of emissivities using our proposed technique.

Gonzalo CP et al.: Finding the magnetopause location using soft X-ray observations and a statistical inverse method

associated with small data variability (blue box length). Similar to the results obtained with synthetic measurements, this study shows the dependence of 3-D estimations on the vantage point and a significant improvement when measurements are acquired from perpendicular locations to the Sun−Earth line.

With a similar format to Figures 14, Figure 15 shows the calculated values of error in the magnetopause location using the two methods described in Section 2.2. The results reveal that underestima-
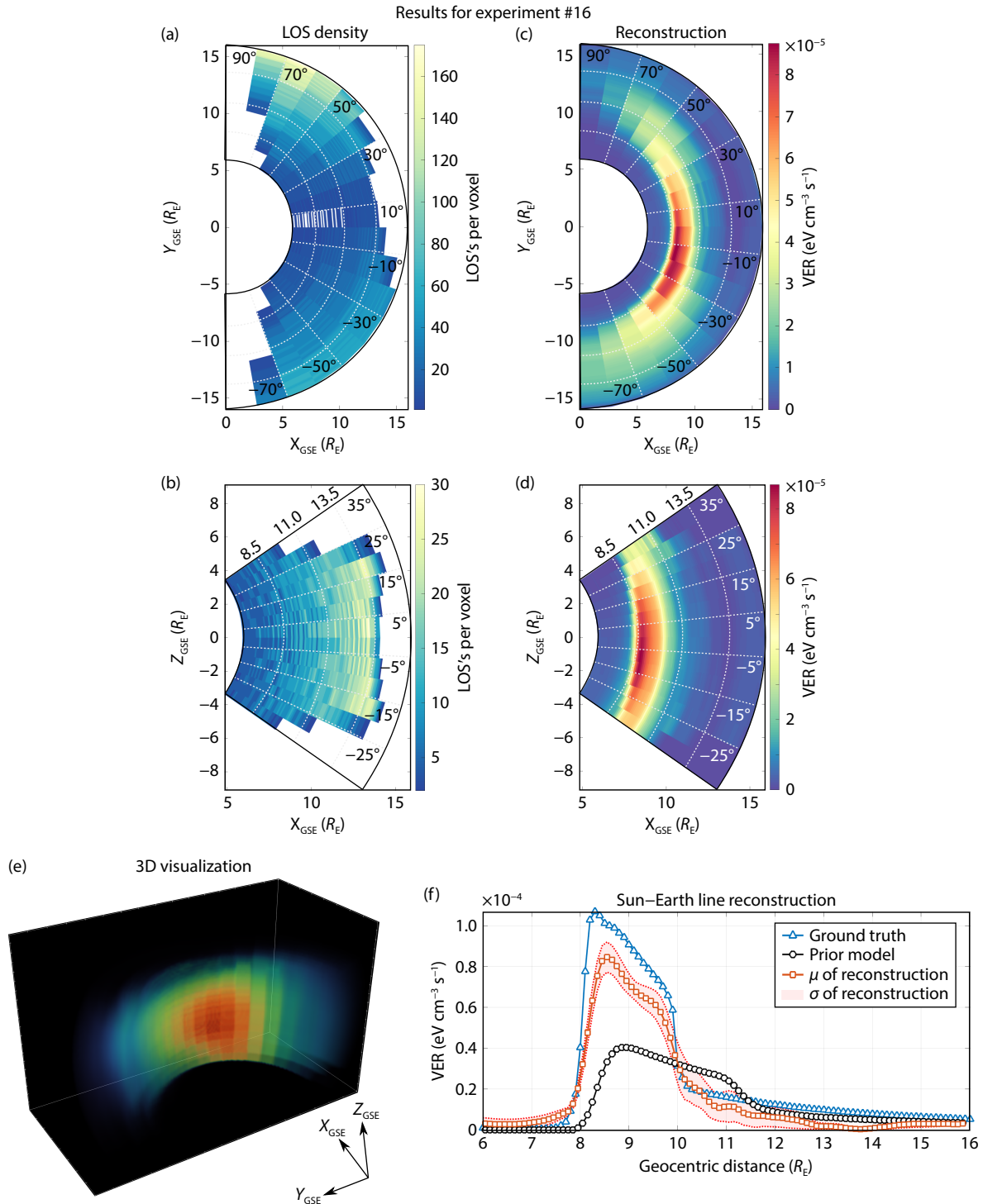

Figure 13. Reconstructions of experiment 16 using realistic synthetic soft X-ray measurements. Panels a and b display the meridional and ecliptic planes of LOS density per voxel, respectively. Panels c, d and e show the meridional and ecliptic planes and a 3-D visualization of estimated soft X-ray volumetric emissivities. Panel f depicts soft X-ray emissivities along the Sun−Earth line where the blue line indicates the ground truth, the black line shows the prior model, and the red line and shadow region display the mean and standard deviation, respectively, of 50 estimations of emissivities using our proposed technique.

Gonzalo CP et al.: Finding the magnetopause location using soft X-ray observations and a statistical inverse method

tion of estimated emissivity values due to the Poisson noise and convolution with the PSF adversely affects the calculation of the magnetopause location using method 1. On the other hand, the use of the derivative to locate the magnetopause in method 2 displayed a scale invariance feature and produced low errors and low data variability despite the small values of estimated emissivities.

4. Discussion

Our methodology shows that 3-D estimation of magnetosheath emissivities derived from simulated 2-D soft X-ray images is possible, and its reliability depends on both the satellite viewing geometry and the input prior model. Experiment #1, using two ideal soft X-ray images acquired from $\phi_i = 39°$ (Figure 8), demonstrates that the MAP estimation effectively uses the input data to significantly modify the prior model and achieve emissivity values similar to those from the ground truth (panel e). However, we found that the resulting 3-D spatial structure does not exhibit a good agreement with the original emissivities but displays similarity with the prior model. On the other hand, the results in experiment #16, which used two ideal soft X-ray images acquired from $\phi_i = 87.7°$ (Figure 9), show excellent agreement in magnitude and structure with the ground truth emissivity model (see panel e). To quantitatively conduct a comparison between estimations and identify the mechanisms that may cause the differences in experiments #1 and #16, we calculated the RMSE and SSIM values (see Figure 10). A simple visual inspection of such values for experiments that used two (2) images indicates that the best results (i.e., lowest

RMSE and highest SSIM) were obtained when the LEXI instrument was located at azimuthal angles almost perpendicular to the Sun–Earth line (ϕ_i in the range 68.2° to 97.5°). Since all these cases used two LEXI images and had almost identical FOV coverage of the solution domain, we infer that the different results should be mainly attributed to both the LEXI's viewing geometry and the specific spatial distribution of the target's emissivities. The magnetosheath region, which produces the highest soft X-ray emissivities, has a symmetric parabolic structure along the Sun–Earth axis. Although LEXI's FOV is identical for all experiments, in experiment #1, the FOV covers only the dawn side of the magnetosheath, while in experiment #16, the FOV covers the complete dusk-to-dawn structure. Hence, we identify that those regions not observed by the sensor in experiment #1 (i.e., the dusk side) are mainly populated by emissivity values from the prior model, which still influences the zone near the Sun–Earth line, ultimately conveying the structural properties to the estimation presented in Figure 8 panel e. It is noteworthy that this analysis is based on the assumed prior model of emissivities, which, in this study, is purposely different in both structure and magnitude from the ground truth (SSIM = 0.3) in order to assess our algorithm. In a realistic scenario, the prior would be generated using an MHD model such as OpenGGCM as well as solar wind parameters such as density, velocity, and magnetic field reported in the OMNI dataset during the acquisition period. In that sense, the results reported in this manuscript should be carefully considered as a baseline where RMSE and SSIM values may improve if a more sophisticated prior model is used.
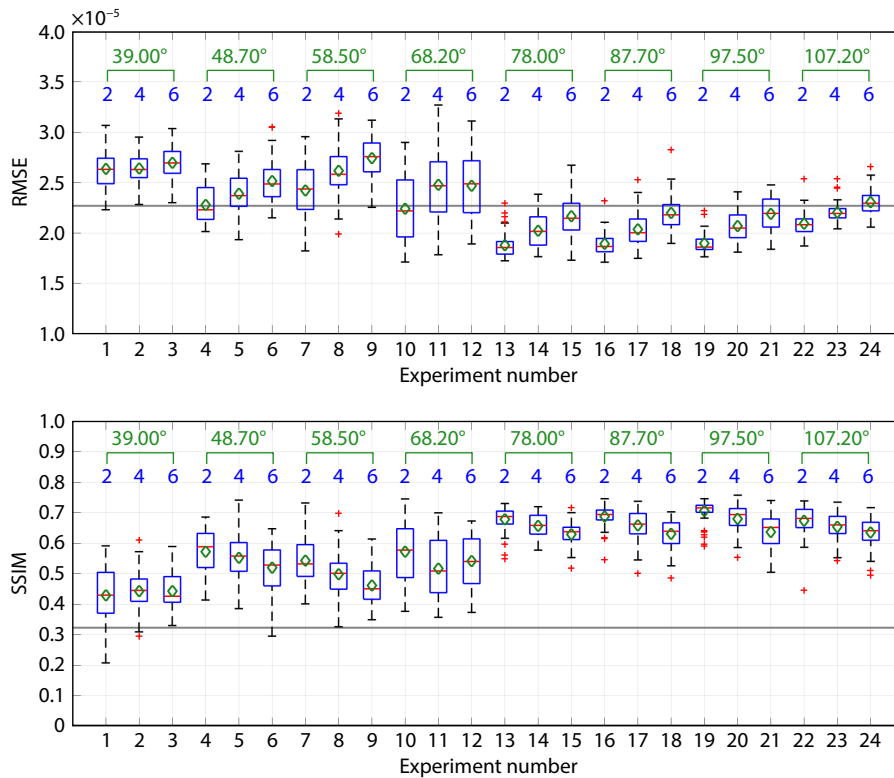

Figure 14. RMSE (top panel) and SSIM (bottom panel) values for each experiment using "realistic" synthetic soft X-ray measurements. The green numbers indicate each experiment's initial angle (ϕ_i), and the blue numbers indicate the number of images used in the 3-D estimations (see text for details).

Gonzalo CP et al.: Finding the magnetopause location using soft X-ray observations and a statistical inverse method
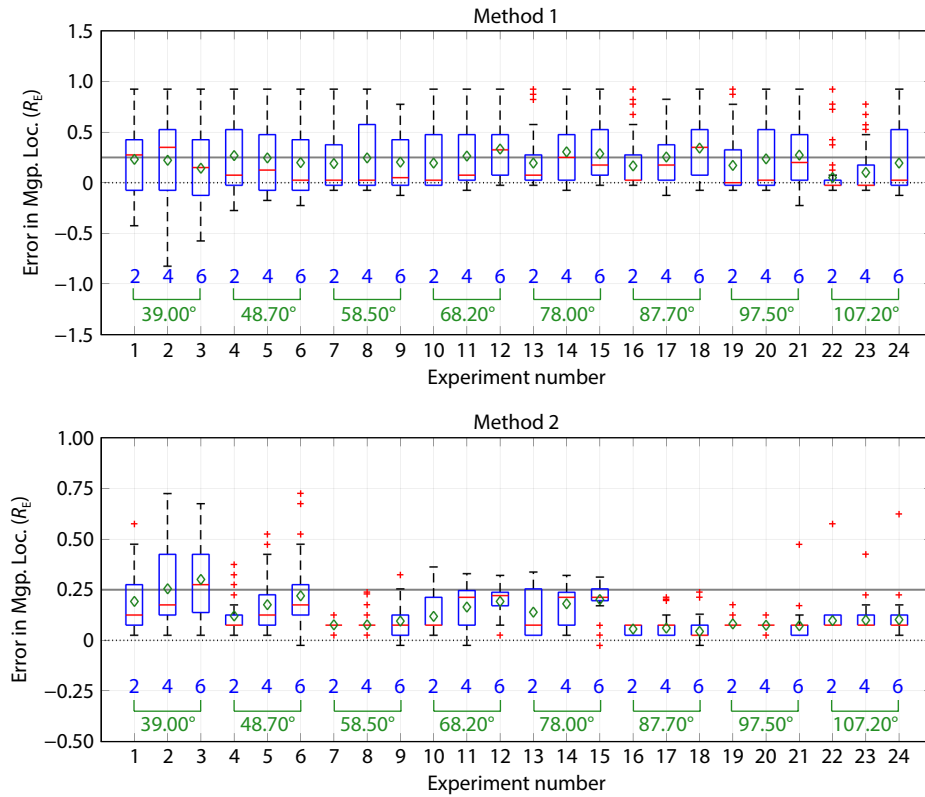
Figure 15. The error in magnetopause location was calculated from 3-D retrievals derived from realistic soft X-ray measurements (see text for details).

The values of RMSE for the ideal experiments reported in the top panel of Figure 10 show a consistent trend of increasing the RMSE with the number of images. This effect can be attributed to the total number of voxels used in the 3-D estimations, which linearly increases with the number of images. These voxels are mainly located near the boundaries of the solution domain, i.e., $r \approx 16\ R_E$, where emissivity values are around one order of magnitude smaller than those in the magnetosheath region. As a result, their estimation is challenging and yields high errors that are introduced to the calculation of the RMSE. To better understand this issue, we performed the analysis of noise-less estimations using 1 to 20 images acquired from $\phi_i = 39°$ and 0.08 degrees separation among them. Figure 16 shows, in a black line, the resulting RMSE (top panel) and SSIM (bottom panel) for these conditions. We found that the abovementioned trend has an inflection point around eight (8) images. When the number of images is greater than 8, the RMSE consistently decays since the viewing geometry for these cases includes voxels with large LOS angle variability, i.e., LOSs in different directions, which ultimately benefits the retrievals. Similarly, the SSIM value increases when the number of images utilized for the estimation process is greater than 8. It is noteworthy that this analysis is specific to the LEXI's viewing geometry and the voxel grid used in this study. Also, since the objective of our study was to evaluate the short-time 3-D estimations, namely less than 1 hour, we do not report results for a number of images greater than 6.

Results for experiments #1 and #16 using two realistic soft X-ray images and presented in Figures 12 and 13 demonstrate that the

technique is capable of reproducing physical structures and reducing the presence of artifacts expected under noisy conditions. Also, emissivity values in panel c (in both figures) are significantly underestimated with respect to ground truth emissivities in Figure 4. This effect is associated with including the PSF over the input data. We observed that the convolution of the soft X-ray image with the PSF kernel significantly reduces the number of counts. In this study, we did not use a deconvolution technique, and it is recommended for investigation as part of future work. Values of RMSE and SSIM reported in Figure 14 and calculated using 50 iterations for each experiment follow similar trends to those estimated with ideal synthetic images, i.e., best results (low RMSE and high SSIM) and lower variability (short box length) are obtained when LEXI instrument is located between 78° to 107.2° azimuthal angle.

In order to analyze the impact of pointing error in our 3-D estimations, we followed a non-sophisticated method to include the expected LEXI's pointing accuracy of 0.3 degrees in the viewing geometry. To do so, we first generate a synthetic image and then enforce a displacement of the pixel values to simulate a pointing error. We implemented two discrete cases in which the pixel values from a synthetic image are moved to one- and two-pixel positions in the right direction, thus emulating 0.25 and 0.5-degree pointing errors only in the longitudinal dimension. In other words, pixel intensity values will adopt erroneous attitude information. Then, we used this new images/attitude data to perform estimations using 1 to 20 images acquired from $\phi_i = 39°$ with a separation of 0.08 degrees among them. In Figure 16, the
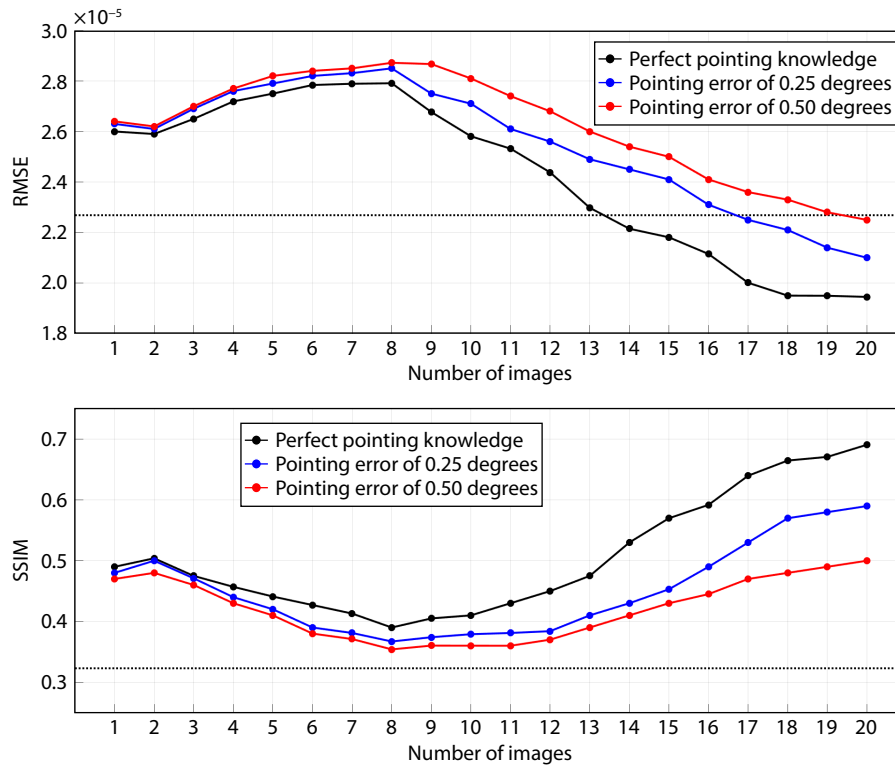
Figure 16. RMSE and SSIM values for 3-D estimations using 1 to 20 images acquired from $\phi_i = 39°$ with 0.08 degrees separation among them. The black line shows the result for perfect pointing knowledge, the blue line shows the results for a pointing error of 0.25 degrees (1-pixel displacement), and the red line shows the results for a pointing error of 0.5 degrees (2-pixel displacement).

blue and red lines show the resulting RMSE (top panel) and SSIM (bottom panel) for 0.25 and 0.5 degrees pointing errors, respectively. The top panel shows that the RMSE values for both cases (blue and red) are slightly larger than the perfect pointing knowledge case (in black) when the number of images is smaller than eight, possibly associated with the large size of the spherical voxels used in our approach as well as the negligible displacement of the spacecraft. However, when more than eight images are used, the RMSE difference between pointing error and perfect knowledge becomes larger as we increase the number of images. This pattern reveals that each additional image (beyond the eighth) used in the estimation process introduces an error in the density estimation that is ultimately accumulated. Also, we acknowledge these results do not only depend on the viewing geometry of the problem but also on the 3-D spatial structure of the target to be estimated. Although this work provides a methodology to assess a 3-D estimations and evaluation of the pointing accuracy, more work should be done when evaluating other voxel grid geometries, a different satellite ephemeris, a time-varying magnetosheath, or the inclusion of Poisson-distributed noise in the images.

The scale used in our estimation method depends on several factors listed here. First, the current technology of soft X-ray imaging sensors may yield low SNR images that restrict the reliable estimation of small-scale structures ($< 0.1 \, R_E$). Second, the ground truth model to be estimated in this study is derived from the OpenGGCM MHD model, which does not provide fine small-scale features near the magnetosheath region; these could be obtained

from more sophisticated models such as global hybrid code (e.g., ANGIE3D) or kinetic-based models (e.g., VLASIATOR) which, in turn, require significantly large computational resources. Finally, the grid used in this study was selected specifically to retrieve large-scale structures such as the magnetosheath and magnetopause location while reducing the computational time in the inversion process. It is noteworthy that the methodology described here is capable of estimating small-scale structures when the abovementioned conditions are met, i.e., high SNR images, small-scale features included in both the ground truth and the prior model, and a high-resolution grid.

Magnetopause location based on the proposed methodology heavily relies on the 3-D estimation. Therefore, the errors in the magnetopause location calculated using both methods and presented for ideal and realistic cases in Figures 11 and 15, respectively, are also affected by the location where LEXI acquires images. It is noteworthy that results in Figure 15, obtained with 50 iterations per experiment, show that method 2 provides the best results in terms of mean/median error (green diamonds/red lines below the reference error = 0.25 R_E) and variability of the estimations (short box length), especially for LEXI positions at $\phi_i \in [58.5°, 107.2°]$.

5. Conclusions and Future Work

In this work, we introduced a statistical-based technique to estimate the 3-D structure of soft X-ray emissivity near the Earth's magnetosheath. This technique, known as maximum a posteriori (MAP) estimation, allows the incorporation of a prior model of

emissivities that deals with the limit-angle observation expected in the LEXI's instrument acquisition. To demonstrate technique feasibility, we generate synthetic measurements using LEXI orbit and attitude and include realistic sources of uncertainty such as Poisson-distributed shot noise, astrophysical background emission, and the effect of the optical point spread function. Reconstruction results show that the technique is robust against systematic noise in the input images. In addition, we found that the accuracy of 3-D estimations highly depends on the observation point. Hence, best results are obtained when the observation is performed perpendicular to the Sun–Earth line. Also, using the prior model of emissivities has a crucial role in the results. In this study, we used a non-sophisticated method to elaborate a prior, but a realistic scenario may use an MHD model or global hybrid code that can improve the results.

Future work includes implementing a 4-D estimation approach to reproduce the dynamic behavior of the magnetosheath and its soft X-ray emissivities. The MAP estimation methodology reported in this manuscript is the basis of dynamic tomography techniques such as Kalman filtering or Optimal Interpolation.

Acknowledgments

References

Aster, R. C., Borchers, B., and Thurber, C. H. (2013). Chapter Eleven-Bayesian methods. In R. C. Aster, et al. (Eds.), *Parameter Estimation and Inverse Problems* (2nd ed., pp. 253-280). Boston: Academic Press. https://doi.org/10.1016/B978-0-12-385048-5.00011-2

Aubry, M. P., Russell, C. T., and Kivelson, M. G. (1970). Inward motion of the magnetopause before a substorm. *J. Geophys. Res.*, 75(34), 7018–7031. https://doi.org/10.1029/JA075i034p07018

Beister, M., Kolditz, D., and Kalender, W. A. (2012). Iterative reconstruction methods in X-ray CT. *Phys. Med.*, 28(2), 94–108. https://doi.org/10.1016/j.ejmp.2012.01.003

Butala, M. D., Hewett, R. J., Frazin, R. A., and Kamalabadi, F. (2010). Dynamic three-dimensional tomography of the solar corona. *Sol. Phys.*, 262(2), 495–509. https://doi.org/10.1007/s11207-010-9536-1

Collier, M. R., and Connor, H. K. (2018). Magnetopause surface reconstruction from tangent vector observations. *J. Geophys. Res.: Space Phys.*, 123(12), 10189–10199. https://doi.org/10.1029/2018JA025763

Connor, H. K., and Carter, J. A. (2019). Exospheric neutral hydrogen density at the nominal 10 R_E subsolar point deduced from XMM-newton X-ray observations. *J. Geophys. Res.: Space Phys.*, 124(3), 1612–1624. https://doi.org/10.1029/2018JA026187

Connor, H. K., Sibeck, D. G., Collier, M. R., Baliukin, I. I., Branduardi-Raymont, G., Brandt, P. C., Buzulukova, N. Y., Collado-Vega, Y. M., Escoubet, C. P., … Zoennchen, J. H. (2021). Soft X-ray and ENA imaging of the earth's dayside magnetosphere. *J. Geophys. Res.: Space Phys.*, 126(3), e2020JA028816. https://doi.org/10.1029/2020JA028816

Cucho-Padin, G., Kameda, S., and Sibeck, D. G. (2022). The Earth's outer exospheric density distributions derived from PROCYON/LAICA UV observations. *J. Geophys. Res.: Space Phys.*, 127(6), e2021JA030211. https://doi.org/10.1029/2021JA030211

Feller, W. (1968). *An Introduction to Probability Theory and Its Applications* (3rd ed). New York, USA: Wiley.

Hajek, B. (2015). *Random Processes for Engineers*. Cambridge: Cambridge University Press.

Jelínek, K., Němeček, Z., and Šafránková, J. (2012). A new approach to magnetopause and bow shock modeling based on automated region identification. *J. Geophys. Res.: Space Phys.*, 117(A5), https://doi.org/10.1029/2011JA017252

Jorgensen, A. M., Sun, T. R., Wang, C., Dai, L., Sembay, S., Zheng, J. H., and Yu, X. Z. (2019a). Boundary detection in three dimensions with application to the smile mission: The effect of model-fitting noise. *J. Geophys. Res.: Space Phys.*, 124(6), 4341–4355. https://doi.org/10.1029/2018JA026124

Jorgensen, A. M., Sun, T. R., Wang, C., Dai, L., Sembay, S., Wei, F., Guo, Y. H., and Xu, R. L. (2019b). Boundary detection in three dimensions with application to the SMILE mission: The effect of photon noise. *J. Geophys. Res.: Space Phys.*, 124(6), 4365–4383. https://doi.org/10.1029/2018JA025919

Jorgensen, A. M., Xu, R., Sun, T., Huang, Y., Li, L., Dai, L., and Wang, C. (2022). A theoretical study of the tomographic reconstruction of magnetosheath X-ray emissions. *J. Geophys. Res.: Space Phys.*, 127(4), e2021JA029948. https://doi.org/10.1029/2021JA029948

Karl, W. C. (2005). Regularization in image restoration and reconstruction. In A. Bovik (Ed.), *Handbook of Image and Video Processing* (2nd ed., pp. 183-202). Boston: Academic Press. https://doi.org/10.1016/B978-012119792-6/50075-9

Kuntz, K. D., Collado-Vega, Y. M., Collier, M. R., Connor, H. K., Cravens, T. E., Koutroumpa, D., Porter, F. S., Robertson, I. P., Sibeck, D. G., … Walsh, B. M. (2015). The solar wind charge-exchange production factor for hydrogen. *Astrophys. J.*, 808(2), 143. https://doi.org/10.1088/0004-637X/808/2/143

Nakano, S., Fok, M. C., Brandt, P. C., and Higuchi, T. (2014). Estimation of the helium ion density distribution in the plasmasphere based on a single IMAGE/EUV image. *J. Geophys. Res.: Space Phys.*, 119(5), 3724–3740. https://doi.org/10.1002/2013JA019733

Paw, C. K., Walsh, B., Kuntz, K. D., Nutter, R., Connor, C., Busk, S., Burwitz, V., Hartner, G., Müller, T., … Thomas, N. (2022). X-ray micropore optic array preliminary calibration results for the lunar environment heliospheric X-ray imager. In *Proceedings Volume 12181, Space Telescopes and Instrumentation 2022: Ultraviolet to Gamma ray* (pp. 121814N). Montréal: SPIE. https://doi.org/10.1117/12.2629503

Raeder, J., McPherron, R. L., Frank, L. A., Kokubun, S., Lu, G., Mukai, T., Paterson, W. R., Sigwarth, J. B., Singer, H. J., and Slavin, J. A. (2001). Global simulation of the Geospace Environment Modeling substorm challenge event. *J. Geophys. Res.: Space Phys.*, 106(A1), 381–395. https://doi.org/10.1029/2000JA000605

Raeder, J., Larson, D., Li, W. H., Kepko, E. L., and Fuller-Rowell, T. (2008). OpenGGCM simulations for the THEMIS mission. *Space Sci. Rev.*, 141(1), 535–555. https://doi.org/10.1007/s11214-008-9421-5

Robertson, I. P., and Cravens, T. E. (2003). X-ray emission from the terrestrial magnetosheath. *Geophys. Res. Lett.*, 30(8), 1439. https://doi.org/10.1029/2002GL016740

Samsonov, A., Carter, J. A., Read, A., Sembay, S., Branduardi-Raymont, G., Sibeck, D., and Escoubet, P. (2022a). Finding magnetopause standoff distance using a soft X-ray imager: 1. magnetospheric masking. *J. Geophys. Res.: Space Phys.*, 127(12), e2022JA030848. https://doi.org/10.1029/2022JA030848

Samsonov, A., Sembay, S., Read, A., Carter, J. A., Branduardi-Raymont, G., Sibeck, D., and Escoubet, P. (2022b). Finding magnetopause standoff distance using a soft X-ray imager: 2. methods to analyze 2-D X-ray images. *J. Geophys. Res.: Space Phys.*, 127(12), e2022JA030850. https://doi.org/10.1029/2022JA030850

Sherman, J., and Morrison, W. J. (1950). Adjustment of an inverse matrix corresponding to a change in one element of a Given Matrix. *Ann. Math. Statist.*, 21(1), 124–127. https://doi.org/10.1214/aoms/1177729893

Shue, J. H., Song, P., Russell, C. T., Steinberg, J. T., Chao, J. K., Zastenker, G., Vaisberg, O. L., Kokubun, S., Singer, H. J., ... Kawano, H. (1998). Magnetopause location under extreme solar wind conditions. *J. Geophys. Res.: Space Phys.*, *103*(A8), 17691–17700. https://doi.org/10.1029/98JA01103

Sibeck, D. G., Allen, R., Aryan, H., Bodewits, D., Brandt, P., Branduardi-Raymont, G., Brown, G., Carter, J. A., Collado-Vega, Y. M., ... Wing, S. (2018). Imaging plasma density structures in the soft X-rays generated by solar wind charge exchange with neutrals. *Space Sci. Rev.*, *214*(4), 79. https://doi.org/10.1007/s11214-018-0504-7

Sun, T. R., Wang, C., Connor, H. K., Jorgensen, A. M., and Sembay, S. (2020). Deriving the magnetopause position from the soft X-ray image by using the tangent fitting approach. *J. Geophys. Res.: Space Phys.*, *125*(9), e2020JA028169. https://doi.org/10.1029/2020JA028169

Tyurin, I. S. (2009). On the accuracy of the Gaussian approximation. *Dokl. Math.*, *80*(3), 840–843. https://doi.org/10.1134/S1064562409060155

Walsh, B. M., Collier, M. R., Kuntz, K. D., Porter, F. S., Sibeck, D. G., Snowden, S. L., Carter, J. A., Collado-Vega, Y., Connor, H. K., ... Thomas, N. E. (2016). Wide field-of-view soft X-ray imaging for solar wind-magnetosphere interactions. *J. Geophys. Res.: Space Phys.*, *121*(4), 3353–3361. https://doi.org/10.1002/2016JA022348

Wang, R. C., Li, D. L., Sun, T. R., Peng, X. D., Yang, Z., and Wang, J. Q. (2023). A 3D magnetospheric CT reconstruction method based on 3D GAN and supplementary limited-angle 2D soft X-ray images. *J. Geophys. Res.: Space Phys.*, *128*(1), e2020JA028169. https://doi.org/10.1029/2022JA030424